Chapter 4

Building Facade Analysis - Elastic

4.1 Introduction

Chapters 4 and 5 of this thesis describe a study undertaken to investigate the response of building facades to ground displacements using finite element analysis. The results of the study are used to develop a new constitutive model for surface beams for the modelling of building facades, such that the beam response closely approximates the behaviour of full facades in soil-structure interaction situations.

As discussed in Chapters 2 and 3, it is common practice in soil-structure interaction problems studied using 2D analysis, to approximate a building as a beam on the ground surface. Current methods of assigning properties to surface beams to model masonry structures are generally not based on any rigorous analysis of the response of buildings to ground movements. Usually, simple linear elastic isotropic properties are assigned to the beam. Burland and Wroth (1974), however, noted that openings in a facade may impact its response to settlements, but provided no rigorous design guidance.

The work described here involves an investigation into the appropriateness of assigning simple elastic properties; finds that for certain building facades current methods could be improved; and goes on to establish a new method for modelling a two-dimensional masonry facade as a surface beam for use in three-dimensional finite element analyses.

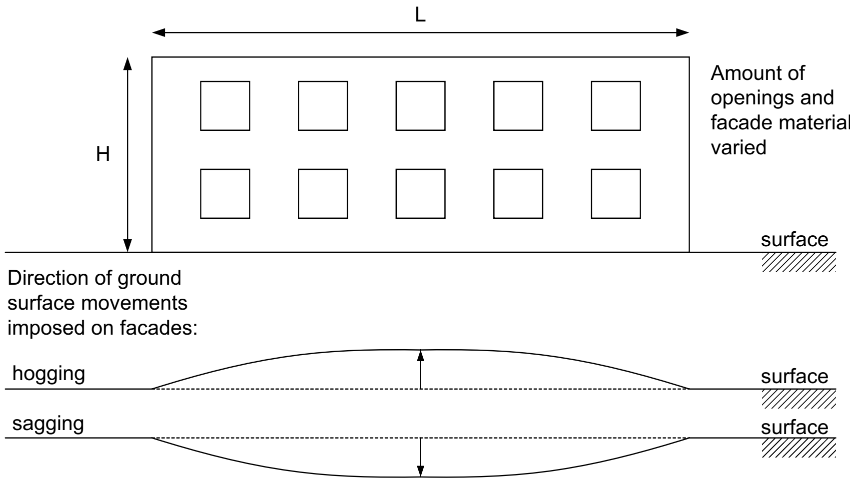

Figure 4.1: **Typical facade with indication of ground movements causing hogging or sagging**

Table 4.1: **Finite element analyses**

Analysis Family	Material	No. Analyses	L/H Ratio range	Openings (%)
E1	Elastic	14	0.75-7.5	Nil
E3	Elastic	14	0.75-7.5	18.750
E5	Elastic	14	0.75-7.5	9.375
E7	Elastic	14	0.75-7.5	6.250
M1	Masonry	28	0.75-7.5	Nil
M3	Masonry	28	0.75-7.5	18.750
M5	Masonry	28	0.75-7.5	9.375
M7	Masonry	28	0.75-7.5	6.250

Factors which influence the interaction between a facade and ground movements considered in this study include: the facade material, overall dimensions, amount and layout of openings, and whether the ground movements cause hogging or sagging of the facade. The influence of these factors are determined by the modelling of both linear elastic and masonry facades which have a range of dimensions and differing amounts of openings. A typical facade with examples of ground displacement is shown in figure 4.1.

A description of the finite element method is not given in this thesis as it is reported extensively in the literature. References on finite element analysis methods used by the author throughout this project include Astley (1992) and Cook et al. (1989).

The study described in Chapters 4 and 5 comprises two series of different finite element analyses; one series for facades with linear elastic material properties (described in Chapter 4) and one for facades made from a non-linear no-tension 'masonry' material (described in Chapter 5). Table 4.1 gives an overview of the finite element analyses performed for this study and the overall range of key parameters considered; a detailed description of all analyses is included in sections 4.2 and 5.3. In each of Chapters 4 and 5, a description of each series of analyses is followed by a critical evaluation of the results and a comparison with current methods of modelling these facades as beams. A new procedure for determining elastic properties to attribute to beams called the *equivalent elastic beam* method is developed based on the results of the analyses with the linear elastic facades in Chapter 4. A new non-linear *equivalent masonry beam* model is developed based on the masonry facade analyses described in Chapter 5.

4.2 Finite element analysis of elastic facades

4.2.1 Introduction

This section describes finite element analyses of building facades where a linear elastic facade material is assumed. An outline of the analyses performed is followed by presentation and discussion of the results.

4.2.2 Software

All finite element analyses in this project were undertaken using the Oxford University Civil Engineering Research Group in-house finite element software OXFEM. This software is written in FORTRAN 90 and was originally developed by Burd (1986) and Houlsby but has since been supplemented by numerous research students including Augarde (1997), Liu (1997), Bloodworth (2002) and Wisser (2002). A good description of its origin and development is given by Bloodworth (2002). A description of the numerical techniques used in the solution of finite element problems in OXFEM is given in section 7.5. Mesh generation and post-processing were undertaken using external programs as described below.

4.2.3 Facade meshes

A description of the full range of elastic facades analysed is given in table 4.2 and the facade meshes are shown in Appendix A. The commercial software package I-DEAS, produced by the Structural Dynamics Research Corporation was used for mesh generation. The simulation application within the I-DEAS software was found to be acceptable by Liu (1997) and Augarde (1997) for generating meshes for geotechnical problems involving buildings.

Groups of facades with similar amounts of openings representing windows are grouped into *families* in table 4.2. Families E5 and E7 have some facades with slightly different percentages of openings due to geometrical constraints.

Once the geometry of each facade was defined, a modular form of mesh generation was used rather than using the *mapped* or *free* meshing facilities in I-DEAS as these can both lead to inconsistencies in meshes repeatedly generated for similar facades of differing sizes. This method facilitated mesh generation for the large number of analyses with different geometries and ensured consistency such that mesh differences were not a cause of error.

The modular method involved the design of a mesh block which could be repeated to form full facade meshes. Two mesh blocks were designed, one with a window and one without. A *crossed triangle* form of mesh with six noded plane triangle elements was chosen to maintain symmetry. Both blocks were constructed manually in I-DEAS by specifying nodal coordinates. The blocks are shown in figures 4.2 (a) and (b). The block containing the window comprises 106 nodes and 56, six noded, linear strain triangle elements, while the no-window block contains 104 nodes and 64 elements. Full facades constructed by the repetition of the blocks are shown in Appendix A, which contains all the facades analysed which included window openings. Facades without windows are listed in table 4.2 and comprise the appropriate number of plain mesh blocks. The two examples shown in figures 4.3 and 4.4 are meshes for analyses E13 (no windows) and E33 (18.75% windows).

The meshed facades were exported from I-DEAS to ABAQUS (the commercial finite element software) format and then to a format readable as input files by OXFEM by using the CONVERT FACADE program written by Augarde (1997). These files contain node

Table 4.2: **Schedule of facade meshes for elastic analyses**

Facade Family	**Facade Number**	**Length (m)**	**Height (m)**	**L/H Ratio**	**Openings (%)**
E1	E11	60	8	7.50	0
E1	E12	40	8	5.00	0
E1	E13	20	8	2.50	0
E1	E14	40	12	3.33	0
E1	E15	20	12	1.67	0
E1	E16	20	16	1.25	0
E1	E17	12	16	0.75	0
E3	E31	60	8	7.50	18.750
E3	E32	40	8	5.00	18.750
E3	E33	20	8	2.50	18.750
E3	E34	40	12	3.33	18.750
E3	E35	20	12	1.67	18.750
E3	E36	20	16	1.25	18.750
E3	E37	12	16	0.75	18.750
E5	E51	60	8	7.50	9.375
E5	E52	40	8	5.00	9.375
E5	E53	20	8	2.50	9.375
E5	E54	40	12	3.33	10.000
E5	E55	20	12	1.67	10.000
E5	E56	20	16	1.25	9.375
E5	E57	12	16	0.75	9.375
E7	E71	60	8	7.50	5.625
E7	E72	40	8	5.00	5.625
E7	E73	20	8	2.50	5.625
E7	E74	40	12	3.33	6.250
E7	E75	20	12	1.67	6.250
E7	E76	20	16	1.25	5.625
E7	E77	12	16	0.75	6.250

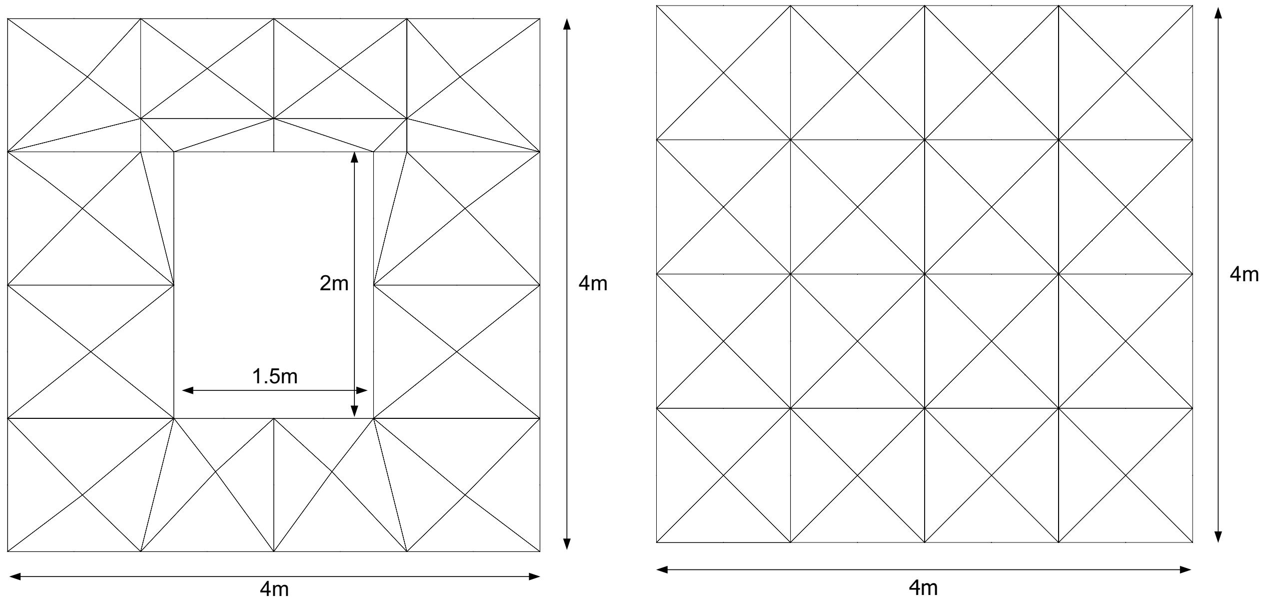

(a) With window (b) Without window

Figure 4.2: **Facade mesh blocks with and without window**

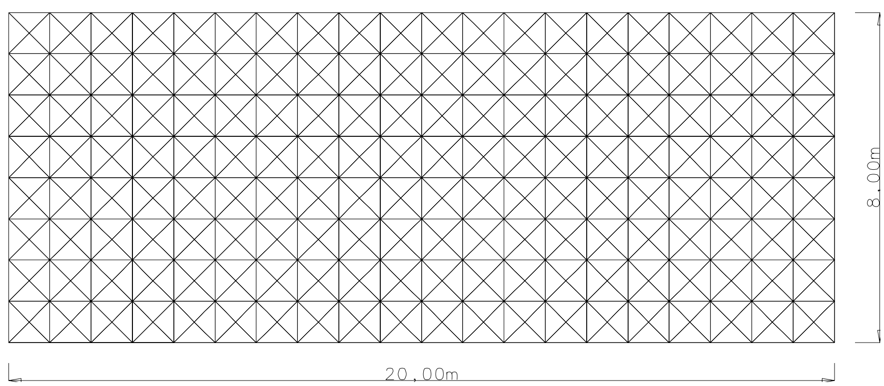

Figure 4.3: **Facade mesh E13, 20m x 8m, no windows**

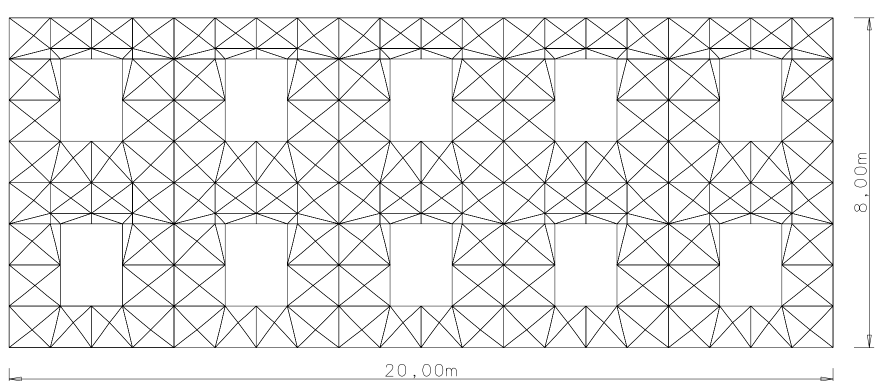

Figure 4.4: **Facade mesh E33, 20m x 8m, 18.75% windows**

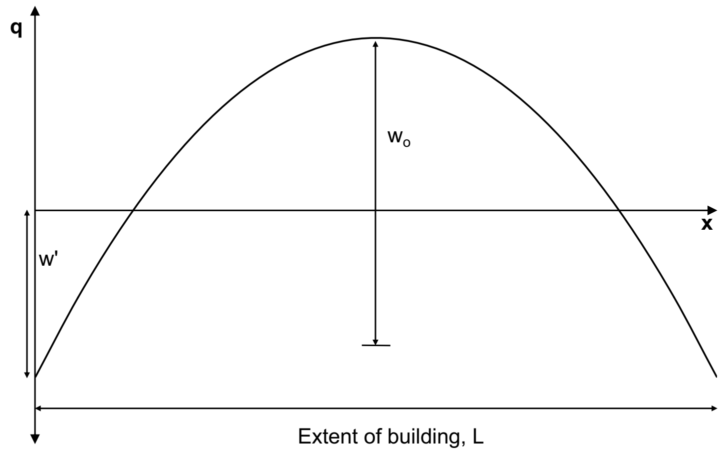

Figure 4.5: **Parabolic load distribution for facade analysis**

and element information, to which is added information about the material, boundary conditions including any ground displacements and options for data output.

4.2.4 Description of elastic finite element analyses

The material properties used for the linear elastic isotropic facades were: Young's modulus E, of 10,000MPa and Poisson's ratio v, equal to 0.2. These properties are typical for masonry when making the assumption that the material is linear elastic (Liu, 1997).

Each of the facades described above was subjected to an imposed displacement at base level. The form of the displacements applied was chosen so that the resulting stresses at the base of the facade could be easily compared to the stresses that would theoretically occur at the base of a linear elastic beam subjected to the same displacements. To facilitate these comparisons, a parabolic load distribution at the base was chosen as the desired result (ignoring self weight) after applying displacements to the facade base as this involves parameters that are convenient for comparison. The form of the parabolic load distribution chosen is shown in figure 4.5. The expression for the parabolic load distribution shown can be written by inspection as,

$$q = \frac{w_o x \left(L - x\right) 4}{L^2} - w' \tag{4.1}$$

where w_o, w' and L are defined in figure 4.5 and x is the distance along the facade base. If the assumption is made that the area under the parabola sums to zero (i.e. the total load applied to the facade is zero), w' can be found to be equal to $2w_o/3$. Utilising the result that $d^2M/dx^2 = q$ (Timoshenko, 1957) where M is the bending moment we can integrate to find the expression for moment as,

$$M = \frac{w_o x^2}{3L^2}\left(2xL - x^2 - L^2\right) \tag{4.2}$$

To derive an expression for the displacement to be applied to give this bending moment and thus the desired parabolic load, an appropriate beam theory must be chosen. The simplest beam theory is Bernoulli-Euler theory (as described by Timoshenko, 1957) where beam displacements are described by assuming that stresses present are those associated with bending only and shear stresses are ignored. The relationship between curvature and moment in this case is,

$$\frac{d^2y}{dx^2} = -\frac{M}{EI} \tag{4.3}$$

where y is the vertical displacement, x is the distance along the beam, d^2y/dx^2 is the curvature, E is the Young's modulus and I is the second moment of area.

This is acceptable for long slender beams, however Timoshenko (1957) notes that where a beam is relatively short or deep, shear effects can be significant. It is considered that shear effects will be significant in the analysis of building facades due to their potentially deep geometries and as a result, such effects should be considered in the derivation of the imposed displacements to be applied to the facades. Beam theory where the analytical solution for the deflection includes shear terms is known as *deep* or *Timoshenko* beam theory after Timoshenko (1957). The relationship between moment and curvature in this case is given by Timoshenko as,

$$\frac{d^2y}{dx^2} = -\frac{1}{EI}\left(M + \frac{EIq}{kAG}\right) \tag{4.4}$$

where E is the Young's modulus, I is the second moment of area, k is a shape factor (used to correct for shear averaging through a cross-section; see section 6.2) equal to 2/3 for a rectangular cross section, A is the cross sectional area, M is the bending moment from equation 4.2 and q is the expression for distributed load from equation 4.1. Further discussion regarding Timoshenko beam theory is given in Chapter 6. Solving for displacement $y(x)$ (using the condition that there is no displacement at either end of the beam to solve for the constants of integration) gives,

$$y(x) = \frac{w_o x(x-L)}{180EIL^2}\left(2x^4 - 4x^3L + x^2L^2 + xL^3 + L^4\right) - \frac{w_o x^2 (x-L)^2}{2AGL^2} \tag{4.5}$$

Two different boundary conditions were analysed. The first, the *rough* case, uses the assumption that the soil will restrain the building facade at ground level leading to the lower boundary being fixed in the horizontal direction. The neutral axis for the facade is thus at the base. The rough case finds support in the literature from Burland and Wroth (1974) in their discussion of settlement related building damage. The second case, called the *smooth* case, assumes that no lateral restraint is provided by the soil at the base and horizontal slip can occur. For the smooth case, the neutral axis is at the mid-height of the facade. Burland et al. (1997) note that the smooth case may be more realistic due to evidence presented of case study buildings where slip occurs at ground level in soil-structure interaction situations. Both cases are analysed here for completeness.

The calculation of second moment of area, I, will differ under each boundary condition regime, leading to different applied displacements for smooth and rough based facades. The displacement regime for each facade comprises the values calculated at each node using equation 4.5. For the elastic analyses, the direction of the imposed displacements is chosen such that, for the smooth case, displacements cause sagging of the facade and for the rough case, applied displacements cause hogging of the facade. These boundary conditions mirror those chosen by Burland and Wroth (1974), who use these two conditions in their analytical investigations. The opposite cases need not be analysed as they will simply produce the negative results of the analysed cases.

Commonly a Gaussian displacement profile is used in studies of tunnelling induced ground movements. The sixth order displacement function described above is used instead in this section of work for two reasons. Firstly, to facilitate ease of comparison of loads arising at the facade base; a parabolic distribution there is convenient for this purpose, and secondly to allow Gaussian ground displacement profiles to be used in the testing and check analyses described in Chapter 6. By using two different displacement profiles in this way it is hoped that the beam models developed in this work will be more robust.

4.2.5 Output and post-processing

Results from OXFEM include the stress and strain results at all Gauss points and nodal values of force and displacement. The desired values for this investigation were, however, the stress values along the base of the facade. These stress values enable the response of the facade to the applied displacements in the finite element analysis to be compared to the analytical response described in equation 4.1. It was therefore necessary to derive expressions to determine the stresses at the base of the facade consistent with the nodal force output. This was done by approximating the stress distribution as a piecewise linear distribution as shown in figure 4.6. Expressions for the nodal forces due to a uniformly and linearly distributed load on an element as shown in figure 4.7 were combined to solve for the stress at each element. The general solution for a facade comprising N elements along its base was found to be,

$$\begin{bmatrix} \frac{5l^2}{36} & \frac{l^2}{9} & 0 & 0 & 0 & \dots & 0 \\ \frac{l^2}{9} & \frac{l^2}{3} & \frac{l^2}{9} & 0 & \dots & 0 & 0 \\ 0 & \frac{l^2}{9} & \frac{l^2}{3} & \dots & 0 & 0 & 0 \\ \vdots & \vdots & \vdots & \ddots & \vdots & \vdots & \vdots \\ 0 & 0 & \dots & 0 & \frac{l^2}{9} & \frac{l^2}{3} & \frac{l^2}{9} \\ 0 & \dots & 0 & 0 & 0 & \frac{l^2}{9} & \frac{5l^2}{36} \end{bmatrix} \begin{bmatrix} \sigma_1 \\ \sigma_2 \\ \vdots \\ \sigma_N \end{bmatrix} = \begin{bmatrix} \frac{Q_0 l}{6} + \frac{P_1}{3} \\ (P_1 + Q_1 + P_2)l/3 \\ \vdots \\ (P_{N-1} + Q_{N-1} + P_N)l/3 \\ \frac{Q_N l}{6} + \frac{P_N}{3} \end{bmatrix} \tag{4.6}$$

where P and Q are nodal forces at the middle and end nodes of the elements respectively (shown in figure 4.6), l is the length of each element and σ_i is the average stress at the base

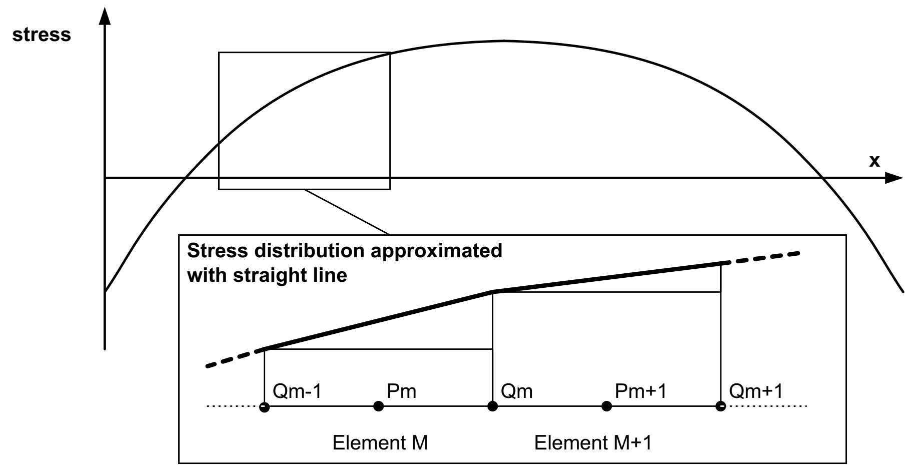

Figure 4.6: **Determination of load distribution at facade base from nodal forces**

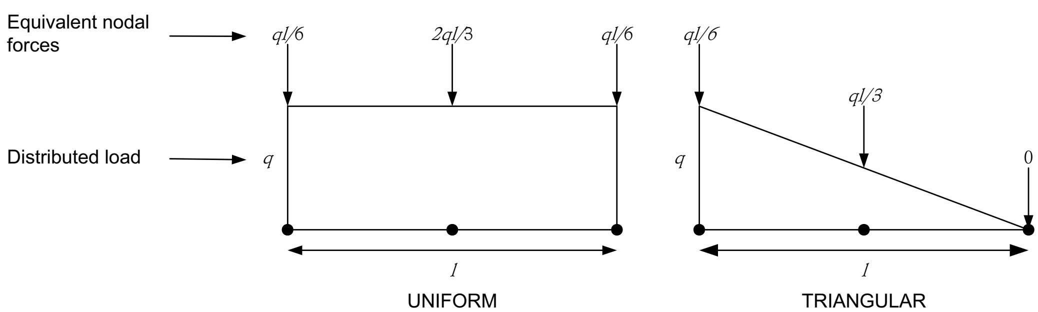

Figure 4.7: **Nodal forces equivalent to uniform and triangular distributed loads**

of element i. This approach required the lengths, l, of all elements to be the same. This equation is solved for the stress at each element which can then be plotted and a parabolic line of best fit assumed (in the form of the distribution shown in figure 4.5).

4.2.6 Results

Finite element stiffness

The results of the finite element analyses of the facades are the stress distributions at the base of the facade. These can be characterised by the intercept value, w' and the difference between the highest and lowest points on the stress curve, w_o defined in figure 4.5. Defining

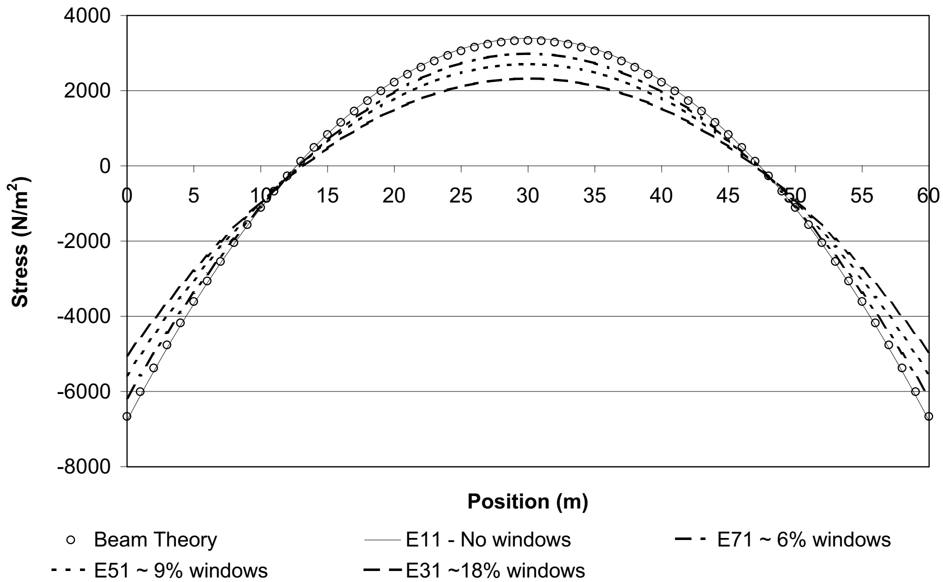

Figure 4.8: **Example stress distributions at facade bases - Effect of increasing % openings**

stiffness, K of the facade as w_o divided by the displacement at the midpoint gives

$$K = \frac{w_o}{y(L/2)} \tag{4.7}$$

where $y(L/2)$ is the vertical applied displacement at the midpoint of a facade of length L. For each facade, define K_{fe} as the *finite element stiffness* which is found using w_o from the finite element analysis results and the applied central displacement, $y(L/2)$ as

$$K_{fe} = \frac{(w_o)_{fe}}{y(L/2)} \tag{4.8}$$

Examples of the stress distributions from which the K_{fe} values are derived are shown in figure 4.8 for 60m long, 8m high facades with differing amounts of openings (facades E11, E31, E51 and E71 in table 4.2).

Theoretical stiffness value for a beam

For a theoretical deep beam of length L we can define the stiffness in a similar manner to equation 4.7, as the stress divided by the displacement at the midpoint. The applied displacement, $y(x)$ is given by equation 4.5. Solving the expression for displacement at the midpoint where $x = L/2$ gives the following (where $C_1 = 11/5760$ and $C_2 = 1/32$)

$$y(L/2) = \frac{w_o L^4}{EI}(C_1) + \frac{w_o L^2}{AG}(C_2) \tag{4.9}$$

Using the definition of stiffness K from equation 4.7 and the result from equation 4.9, we define K_{beam} as the *theoretical stiffness of a beam* as

$$K_{beam} = \frac{w_0}{\frac{w_0 L^4}{EI}(C_1) + \frac{w_0 L^2}{AG}(C_2)} \tag{4.10}$$

which simplifies to

$$K_{beam} = \frac{1}{\frac{L^4 C_1}{EI} + \frac{L^2 C_2}{AG}} \tag{4.11}$$

Presentation of finite element analysis results

For the presentation of results for this phase, the stiffness K_{fe} for each facade is normalised by dividing by the appropriate value of theoretical beam stiffness K_{beam} to obtain a *normalised stiffness ratio* of K_{fe}/K_{beam}. This provides an interesting result as the response of the facade in comparison to the response of a theoretical deep beam (as is commonly used to model such facades described in Chapter 2) can be easily established.

Shown below in figures 4.9 and 4.10 are plots of normalised stiffness ratio against length to height (L/H) ratio for smooth based models in sagging and rough based models in hogging. Each chart contains four plots, one for each family of facades (E1, E3, E5 and E7) with a similar percentage of the face area removed to simulate windows or doors. Percentages of openings over the facade area are not identical within families due to geometrical constraints on the arrangement of the facade mesh blocks used to build the full facades. For this reason, the lines joining the data points in each family are not significant except to indicate trends for facades with similar amounts of openings and for ease of viewing.

A normalised stiffness ratio of unity indicates that the facade is responding to the applied

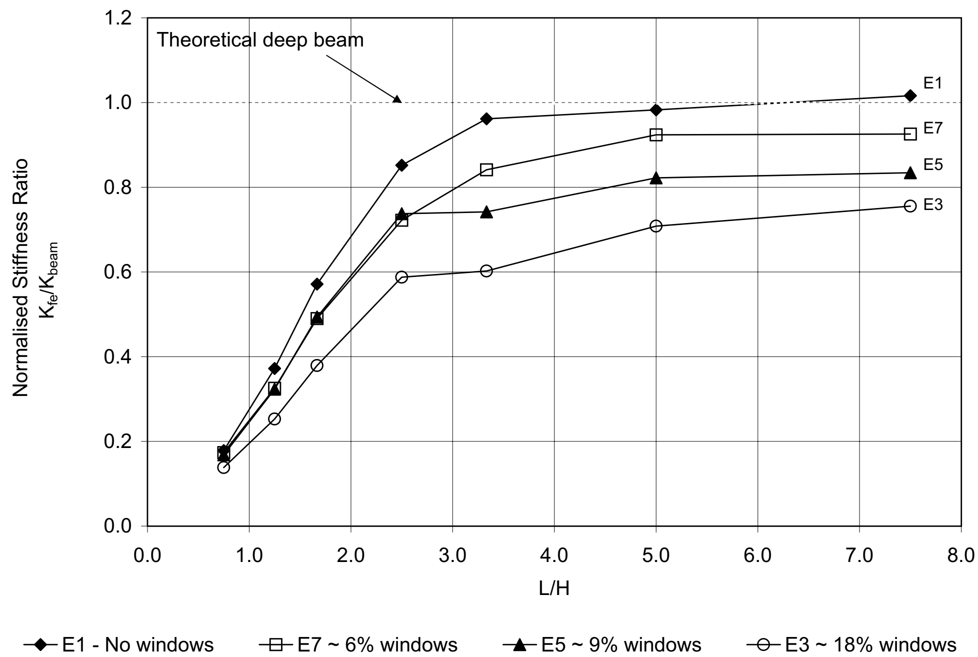

Figure 4.9: **Smooth based facades in sagging - Normalised stiffness ratio**

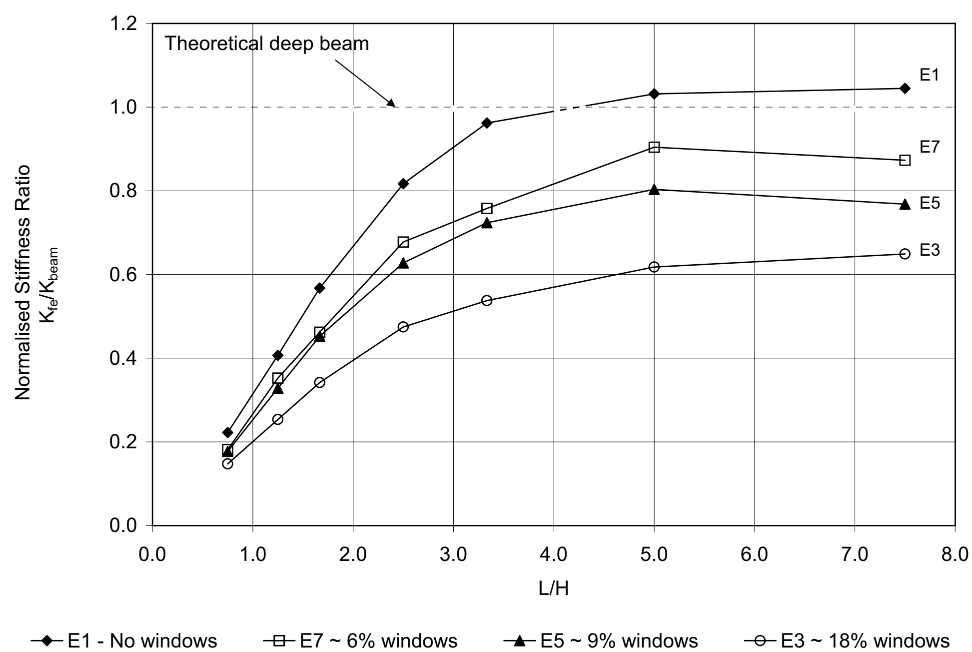

Figure 4.10: **Rough based facades in hogging - Normalised stiffness ratio**

displacement in the same fashion as a theoretical deep beam. Considering facades with no windows initially, family E1 with no windows can be seen to respond in a similar fashion to a deep beam for length to height ratios in excess of about 3.0. As L/H reduces, however, the behaviour deviates from that predicted by beam theory and the normalised stiffness ratio falls, indicating that the finite element model is less stiff than a theoretical deep beam of the same dimensions. The normalised stiffness ratio continues to fall as L/H reduces.

The second factor to consider is the amount of openings in the facade. The effect of increasing the amount of openings in the facades on their response to the applied displacements is evident from the results of families E7, E5 and E3. For facades with identical L/H, as the percentage of windows in the facade increases, a reduction in normalised stiffness ratio is observed. While the results for family E1 with no windows for high values of L/H agree well with the theoretical beam stiffness, facades with openings exhibit decreasing stiffness (the family of curves shifts downwards) as the amount of openings increases.

The charts of normalised stiffness ratio against length to height ratio (L/H) thus appear to exhibit two distinct sections. For high values of L/H, the facade dimensions are such that the only factor causing the response to deviate from that predicted by beam theory is an increasing amount of windows. However for values of L/H less than about 3.0, the overall dimensions of the facade (L and H) have a greater effect on the response than the proportion of windows. This can be seen in the charts by the narrowing in the gap between the response of the windows families, and a simultaneous drop towards the origin in the normalised stiffness plots. From inspection of equation 4.11, K_{beam} can be seen to approach infinity as L/H approaches zero. This causes the normalised stiffness ratio (K_{fe}/K_{beam}) to plot towards zero as L/H falls, assuming that K_{fe} does not tend to infinity in the same way. The possibility that a different mechanism is acting in the finite element analysis at low values of L/H is discussed further in section 4.3.2. The boundary between the section where the percentage of windows is the dominant factor (right hand side) and where the overall dimensions of the facade dominate (left hand side) is denoted the *critical length to height ratio*, $(L/H)_{crit}$. This is observed to occur at a value of approximately $L/H = 3.0$.

The concept of the critical length to height ratio is illustrated in figure 4.11. Each side of the dividing line of $(L/H)_{crit}$ is approximated as linear, giving a bi-linear response for the facade over all ranges of L/H. This concept is later utilised in the development of the new equivalent beam models described in section 4.3.

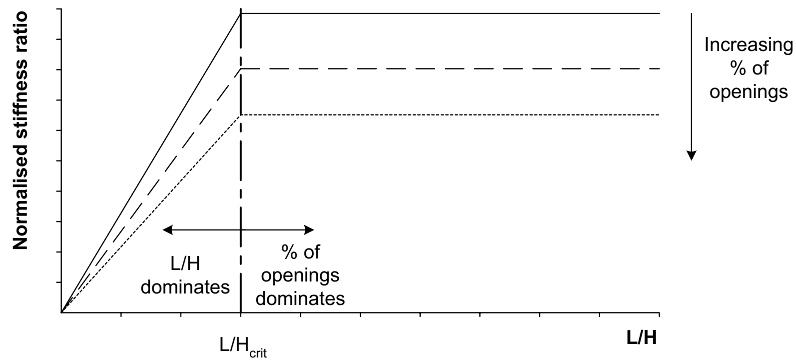

Figure 4.11: **Critical length to height ratio,** $(L/H)_{crit}$

From these results it is evident that the commonly used approximation of a building facade (or building) as a beam with isotropic elastic properties is only appropriate for long, low buildings facades with no openings. For shorter facades or those with openings (or both) the commonly used deep beam with linear elastic properties attributed based on a simple plain wall does not respond to ground displacements in the same manner as the facade. A new method involving a procedure to assign appropriate properties to surface beams therefore needs to be developed such that elastic beams can more accurately represent building facades for all ranges of L/H and for differing amounts of openings.

4.3 Development of equivalent elastic beam method

This section describes the development of a new procedure to assign appropriate properties to elastic surface beams such that they respond to ground movements in a similar manner to elastic building facades of all sizes and with varying amounts of openings. This procedure is called the *equivalent elastic beam* method and it assigns properties to elastic Timoshenko beams as described below. As discussed in section 2.5.2, buildings are subject to both bending and shear effects due to soil settlements and Timoshenko beam theory allows for the inclusion of both (as opposed to Bernoulli-Euler beams with only bending effects). Let the stiffness of such a beam be K_{equiv} and be given by

$$K_{equiv} = \frac{1}{\frac{L^4 C_1}{EI^*} + \frac{L^2 C_2}{A^* G}} \tag{4.12}$$

where C_1 and C_2 are constants given above for equation 4.9 and E and G are the Young's and shear moduli of the material respectively. The values of A^* and I^* are the *effective cross sectional area* and *effective second moment of area* respectively of a building facade with geometric properties A and I. These values, once derived below, will be used as inputs for the shear and bending stiffness of the elastic beam.

The approach developed below, with appropriate bending and shear stiffnesses found for the beam by investigation of geometric properties A and I, differs from the approach of Burland and Wroth (1974) who note that differing amounts of openings may be allowed for by manipulation of the ratio E/G directly. Weaknesses of this E/G ratio approach include: that no guidance is given as to appropriate values of the moduli to use for differing amounts of openings (arbitrary high and low values are chosen for extreme cases only); no modification is given for effects of the overall geometry (L/H) of the buildings, which is required as discovered in the analysis in the previous section; and values of E and G presented are not based on any robust analysis of the soil-structure interaction problem in hand. The new approach attempts to addresses these issues.

The procedures described below are thus concerned with the determination of appropriate effective values, A^* and I^*, from the geometry of any given facade. The aim is to develop a method that gives values such that when the derived A^* and I^* are used in the calculation of K_{equiv} it approximates the stiffness value K_{fe} observed from the results of the finite element analyses. For the presentation of results for this phase, the comparison of the theory and finite element results is again undertaken after normalising stiffness values by dividing by the appropriate value of K_{beam} for the facade dimensions.

Determination of A^* and I^* consists of two stages. Stage 1 consists of a procedure based on the facade geometries to determine value of effective shear area, A^* from consideration of shear (denoted part (a)) and the effective second moment of area, I^* from consideration of bending (denoted part (b)) for deep beams. After this stage, the results are shown to give good agreement between K_{fe} and K_{equiv} for the region where $L/H > (L/H)_{crit}$ (where the amount of openings is the dominant variable) but poor agreement for facades with $L/H < (L/H)_{crit}$. For the region of $L/H < (L/H)_{crit}$ a second stage of analysis is thus added. For Stage 2, two alternative methods have been developed to augment the stage one geometric procedure. The first is denoted the *Linear Depression* method and the second is the *Limiting Height* method. As for the Stage 1 procedure, each alternative Stage 2 model has two parts, part (a) to determine A^* and part (b) to determine I^*. The derivation and detail of these new procedures is described below.

4.3.1 Stage 1 - Geometry based procedure

Part (a) - Shear

Consider a short cantilever beam as shown in figure 4.12(a). For the plain beam, if we make the simplifying assumption that the shear strain γ is uniform throughout the cross section then γ is given by

$$\gamma = \frac{V_s}{L} = \frac{\tau}{G} = \frac{F}{AG} \tag{4.13}$$

where V_s is the vertical displacement due to shear, L is the length, G is the shear modulus, F is the applied force, A is the cross sectional area and τ is the mean shear stress. Thus

$$V_s = \frac{FL}{AG} \tag{4.14}$$

For the beam with openings in figure 4.12(b) composed of n vertical strips (here $n = 3$) where the cross sectional area and length of strip i are A_i and L_i respectively, V_s can be given by

$$V_s = \frac{F}{G}\left(\frac{L_1}{A_1} + \frac{L_2}{A_2} + \cdots + \frac{L_n}{A_n}\right) \tag{4.15}$$

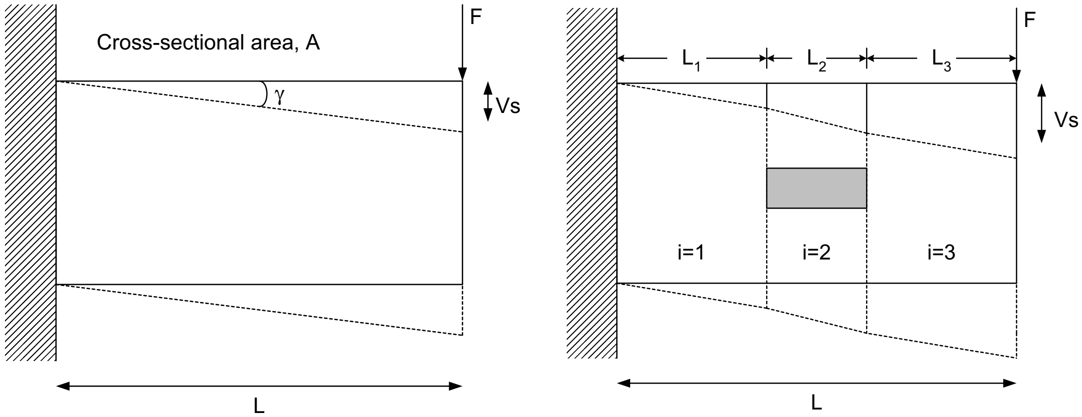

(a) Plain beam (b) Beam with opening

Figure 4.12: **Beams in shear**

where n is the total number of vertical strips and each A_i is net of any openings. For an equivalent deep beam let

$$V_s = \frac{FL}{A^*G} \tag{4.16}$$

such that

$$\frac{FL}{A^*G} = \frac{F}{G}\left(\frac{L_1}{A_1} + \frac{L_2}{A_2} + \cdots + \frac{L_n}{A_n}\right) \tag{4.17}$$

and finally

$$A^* = \frac{L}{\sum_{i=1}^{n}\left(\frac{L_i}{A_i}\right)} \tag{4.18}$$

where A^* is the effective cross-sectional area, L_i is the length of a vertical strip i of facade, A_i is the cross-sectional area of a vertical strip and n is the number of vertical strips.

Part (b) - Bending

Consider a plain beam as shown in figure 4.13(a). The second moment of area I is

$$I = \frac{tH^3}{12} \tag{4.19}$$

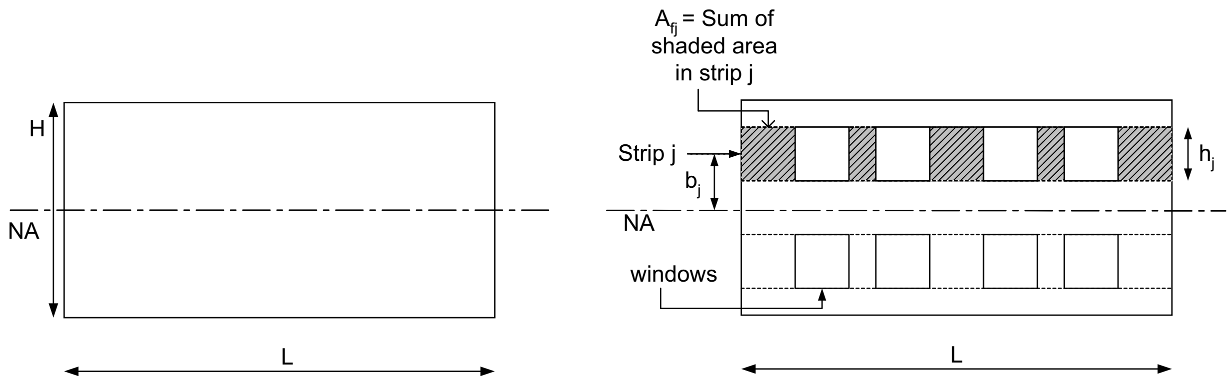

(a) Plain beam (b) Beam with openings

Figure 4.13: **Beams in bending**

where t is the thickness. To calculate the second moment of area for the beam with openings, take n horizontal strips as shown in figure 4.13(b) where strip j has height h_j, face area A_{fj} and thickness t. Take b_j as the distance from the midpoint of the strip to the neutral axis of the facade (shown at the mid-height of the facade, as for a smooth based analysis). To account for the openings, in each strip with windows the effective height h'_j is calculated as $h'_j = A_{fj}/L$, with A_{fj} being the face area of the strip net of windows. For a strip with no windows the effective height h'_j is equal to the height h_j. For each strip the second moment of area I_j is given using the parallel axis theorem as

$$I_j = \frac{t{h'_j}^2}{12} + t h'_j {b_j}^2 \tag{4.20}$$

and the effective second moment of area for an equivalent deep beam is given by

$$I^* = \sum_{j=1}^{n} I_j \tag{4.21}$$

where n is the number of horizontal strips of facade.

Stage 1 Comparison of predicted and finite element results

The values determined for A^* and I^* using the Stage 1 procedure outlined above are used to calculate the stiffness K_{equiv} of a range of equivalent deep beams. These values are compared to the stiffness of the facades K_{fe} from the finite element analyses in the charts shown in figure 4.14. In the figures, normalised stiffness ratios of K_{fe}/K_{beam} and K_{equiv}/K_{beam} are plotted against the length to height ratio (L/H).

From figure 4.14 it can be observed that the geometric Stage 1 procedure gives good agreement with the observed finite element stiffness for high values of L/H. For facade families E1 and E7 (no windows and 5.625% windows respectively) the equivalent beam results closely match the observed finite element response in the high L/H region. For families E5 and E7 with higher percentages of windows, the match is not as close, with approximately a 10% difference on average, but the trend is much better than a theoretical deep beam (normalised stiffness ratio of unity).

For values of L/H below the previously defined critical value of $L/H = 3.0$ however, the equivalent stiffness determined by the procedure above remains far too high in comparison with the finite element response. It is apparent that the geometric Stage 1 method for assigning properties A^* and I^* to equivalent deep beams copes well with the region where the amount of openings dominates the response $(L/H > (L/H)_{crit})$ but not for smaller values of L/H. A second stage of analysis is therefore proposed below to determine more appropriate equivalent beam properties for the region $L/H < (L/H)_{crit}$.

4.3.2 Stage 2 - Methods for facades with $L/H < (L/H)_{crit}$

To determine more appropriate values of A^* and I^* such that the stiffness response of facades with values of L/H less than (L/H_{crit}) is replicated by the equivalent deep beams, two alternative methods are considered.

Method 1 - Linear Depression

In this method the effective values A^* and I^* for facades in the region where $L/H < (L/H)_{crit}$ are calculated as described in stage one above initially but are then multiplied by the ratio of L/H for the model to $(L/H)_{crit}$. This approach makes use of the assumption described in figure 4.11 of a bi-linear normalised stiffness relationship. If the *normalised*

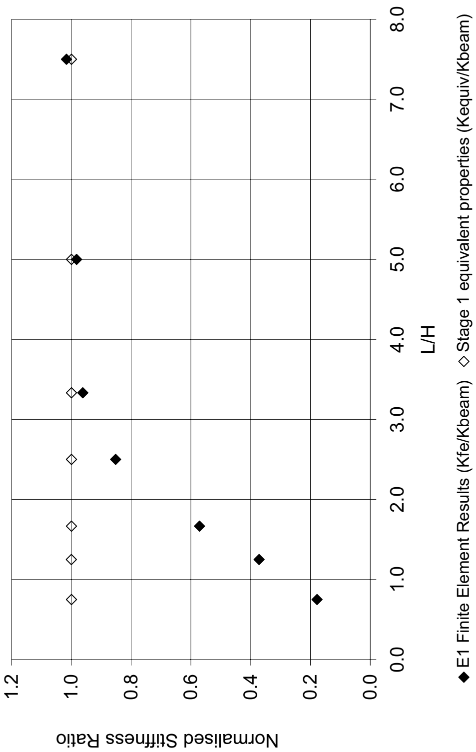

(a) Models E1 - No Windows

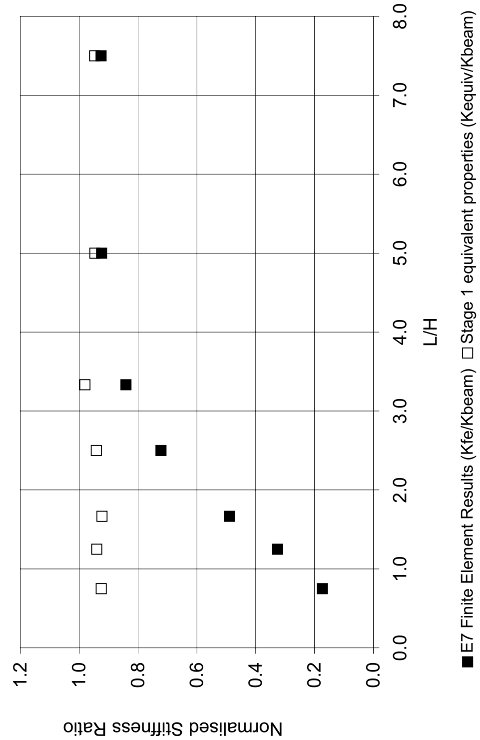

(b) Models E7 - 5.625% Windows

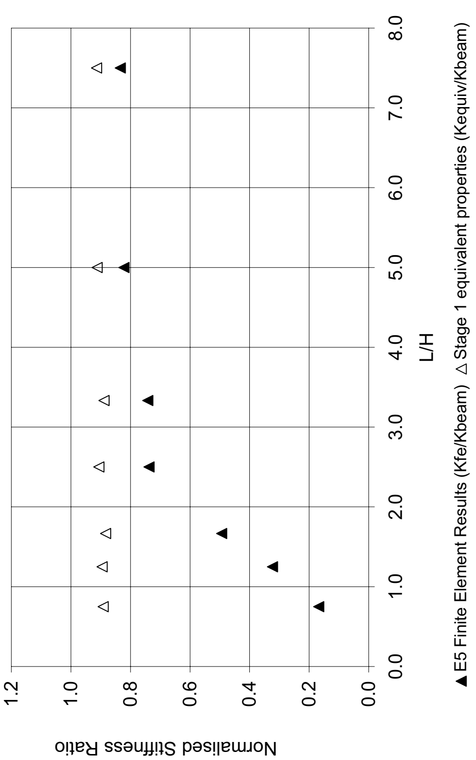

(c) Models E5 - 9.375% Windows

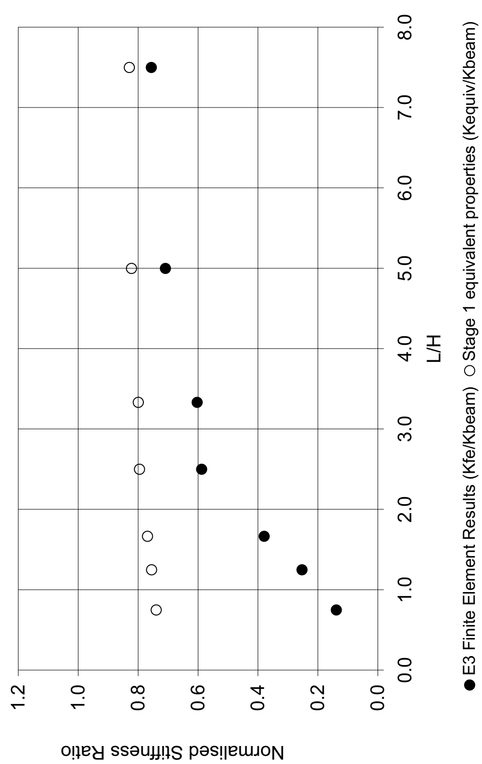

(d) Models E3 - 18.750% Windows

Figure 4.14: **Comparison of finite element stiffness and predicted stiffness from Stage 1 (smooth based)**

stiffness ratio is denoted the NSR, the section from the origin in the normalised stiffness plot to the stiffness value at $(L/H)_{crit}$ under consideration yields the relationship

$$\frac{NSR_{L/H}}{L/H} = \frac{NSR_{(L/H)_{crit}}}{(L/H)_{crit}} \tag{4.22}$$

This same relationship will hold between values of K_{equiv} for different values of L/H less than $(L/H)_{crit}$ and thus values for A^* and I^* can be calculated as

$$A^* = \frac{L}{\sum_{i=1}^{n}\left(\frac{L_i}{A_i}\right)} \times \left[\frac{L/H}{(L/H)_{crit}}\right] \tag{4.23}$$

$$I^* = \left(\sum_{j=1}^{n} I_j\right) \times \left[\frac{L/H}{(L/H)_{crit}}\right] \tag{4.24}$$

Method 2 - Limiting Height

In this alternative method, instead of assuming a straight line relationship to calculate I^* and A^* if $L/H < (L/H)_{crit}$, these quantities are fully recalculated using only a *limiting height*, H_{lim} for the facade equal to $L/3$ above which the facade material is ignored. $L/3$ is chosen as the value for H_{lim} as $(L/H)_{crit}$ is equal to 3.0. The physical interpretation of this approach is the assumption that material is only mobilised in the lower section of the structure when tall structures respond to ground movements. Saint-Venant's principle (Love, 1944) could be said to apply in this case which states that strains produced in a body, due to the application of a system of forces statically equivalent to zero force and zero couple, are of negligible magnitude at distances which are large when compared with the linear dimension. It is as though in this instance the facade starts acting like a long vertical bar, with stresses confined to the base region. In contrast to the Linear Depression method, which is a purely empirical method, the Limiting Height method is thus based on an approximation related to the assumed mechanics of the situation.

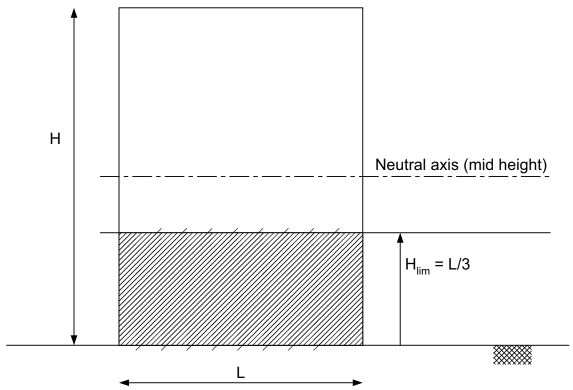

Figure 4.15: **Method 2 - Limiting Height**

These assumptions lead to I^* and A^* being calculated for $L/H < (L/H)_{crit}$ as

$$A^* = \frac{L}{\sum_{i=1}^{n}\left(\frac{L_i}{A_{i_{lim}}}\right)} \tag{4.25}$$

$$I^* = \sum_{j=1}^{n} I_{j_{lim}} \tag{4.26}$$

where $A_{i_{lim}}$ is the cross sectional area of a vertical strip calculated using H_{lim}. $I_{j_{lim}}$ is the second moment of area of a horizontal strip calculated using H_{lim}. For the calculation of $I_{j_{lim}}$ the neutral axis about which the moment is taken is assumed to remain unchanged (at the mid-height of the full facade for smooth based facades and at the base for rough facades). This concept is described in figure 4.15.

4.3.3 Comparison of predicted and finite element results

The predicted stiffness using the values of A^* and I^* produced by both stage two methods described above as well finite element stiffness values are given in table 4.3 for the smooth based facades in sagging. Results are given under headings of the two Stage 2 methods, but it should be noted that the values of A^*, I^* and stiffness K_{equiv} for facades with $L/H > 3.0$ are the same under each method as it is only below $(L/H)_{crit}$ that the additional (and differing) Stage 2 procedures apply. Stiffnesses predicted by each method are normalised (by dividing the stiffness by K_{beam}) and plotted in figures 4.16 and 4.17 along with the observed stiffness from the finite element analyses for each family of facades.

On inspection of figures 4.16 and 4.17 for the region $L/H < (L/H)_{crit}$, both the Limiting Height and the Linear Depression method can be seen to give reasonable agreement with the observed stiffness values from the finite element analyses. Both methods, however, give values slightly higher than the finite element stiffness, for low values of L/H. On comparing the two methods, the Linear Depression method, can be seen from figures 4.16 and 4.17 to give stiffness values slightly closer to those observed. This method is also the simpler of the two to calculate and as such is chosen as the most appropriate method.

A series of analyses with rough bases and a hogging displacement were undertaken, but tables and charts of the results of the predicted and finite element stiffness values of these have not been presented. The results, however, again indicated that new procedure produces appropriate beam properties that give stiffness values in reasonable agreement with the observed finite element results.

4.4 Conclusion

A new approach for assigning material properties to elastic beams to more accurately model building facades of varying dimensions and amounts of openings has been developed. The effective properties A^* and I^* are determined using the new process which is based on geometric criteria and are used in conjunction with the material properties to give the stiffness EI^* in bending, GA^* in shear and EA^* axially. This approach is based on effective geometric properties of the beams rather than material properties (as suggested by Burland and Wroth (1974)) and is thus felt to be more robust. This process is shown to be equally valid for both a smooth or a rough base boundary condition assumption. Assessments of the ability of elastic beams with these properties to model facades in finite element analyses of tunnelling are given in Chapter 8 and Chapter 9.

Table 4.3: **Predicted and observed stiffness - Smooth facades in sagging**

Facade Details			**Predicted Method 1 Linear depression**			**Predicted Method 2 Limiting height**			**Obs. F.E.A.**
Model	L/H	**Gaps (%)**	A^* (m^2)	I^* (m^4)	K_{equiv1} (MN/m^2)	A^* (m^2)	I^* (m^4)	K_{equiv2} (MN/m^2)	K_{fe} (MN/m^2)
E11	7.50	0.000	8.00	42.67	16.29	8.00	42.67	16.29	16.56
E12	5.00	0.000	8.00	42.67	77.17	8.00	42.67	77.17	75.83
E14	3.33	0.000	12.00	144.00	227.53	12.00	144.00	227.53	218.80
E13	2.50	0.000	6.67	35.56	763.72	6.67	27.65	643.12	780.83
E15	1.67	0.000	6.67	80.00	1202.00	6.67	72.10	1144.43	1235.88
E16	1.25	0.000	6.67	142.22	1504.11	6.67	169.88	1587.63	1343.03
E17	0.75	0.000	4.00	85.33	3160.49	4.00	149.33	3372.48	2252.99
E31	7.50	18.750	5.82	35.66	13.51	5.82	35.66	13.51	12.31
E32	5.00	18.750	5.82	35.66	63.40	5.82	35.66	63.40	54.66
E34	3.33	18.750	8.73	118.49	181.78	8.73	118.49	181.78	137.04
E33	2.50	18.750	4.85	29.72	607.16	4.57	21.76	485.32	538.50
E35	1.67	18.750	4.85	65.83	923.42	4.57	59.29	853.47	819.95
E36	1.25	18.750	4.85	116.38	1134.69	4.57	139.15	1141.71	912.50
E37	0.75	18.750	2.91	69.83	2336.67	2.91	121.83	2476.75	1747.51
E51	7.50	9.375	7.11	39.05	14.89	7.11	39.05	14.85	13.59
E52	5.00	9.375	7.11	39.05	70.39	7.11	39.05	70.39	63.44
E54	3.33	10.000	10.50	128.63	202.30	10.50	128.63	202.30	168.78
E53	2.50	9.375	5.93	32.54	691.97	5.82	24.51	567.37	676.01
E55	1.67	10.000	5.84	71.46	1061.90	5.82	64.39	1009.63	1068.03
E56	1.25	9.375	5.93	129.30	1346.39	5.82	152.00	1394.85	1166.51
E57	0.75	9.375	3.56	77.53	2818.28	3.20	130.95	2719.31	2124.80
E71	7.50	5.625	7.44	40.47	15.43	7.44	40.47	15.43	15.08
E72	5.00	5.625	7.44	40.47	73.03	7.44	40.47	73.03	71.27
E74	3.33	6.250	11.16	143.50	223.13	11.16	143.50	223.12	191.40
E73	2.50	5.625	6.20	33.73	719.55	6.12	25.70	595.53	661.86
E75	1.67	6.250	6.12	74.30	1108.99	6.12	66.96	1056.50	1059.98
E76	1.25	5.625	6.20	136.69	1413.85	6.12	158.15	1463.31	1174.69
E77	0.75	6.250	3.69	80.14	2924.72	3.20	130.95	2719.31	2192.50

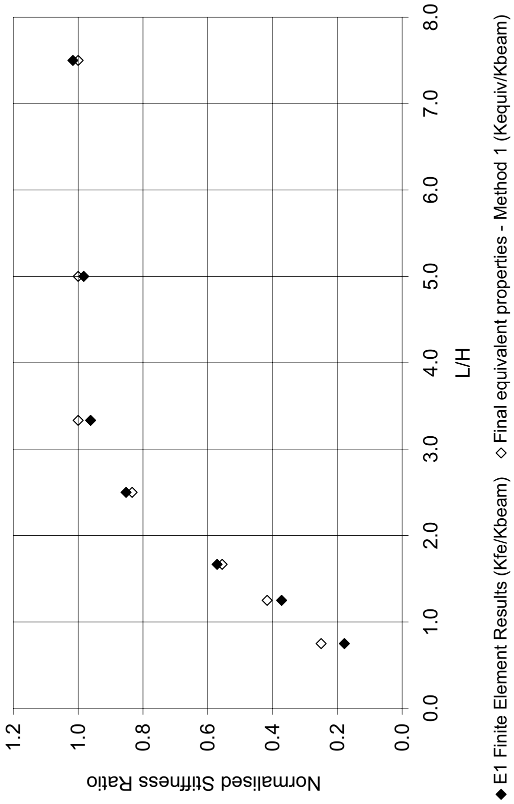

(a) Models E1 - No Windows

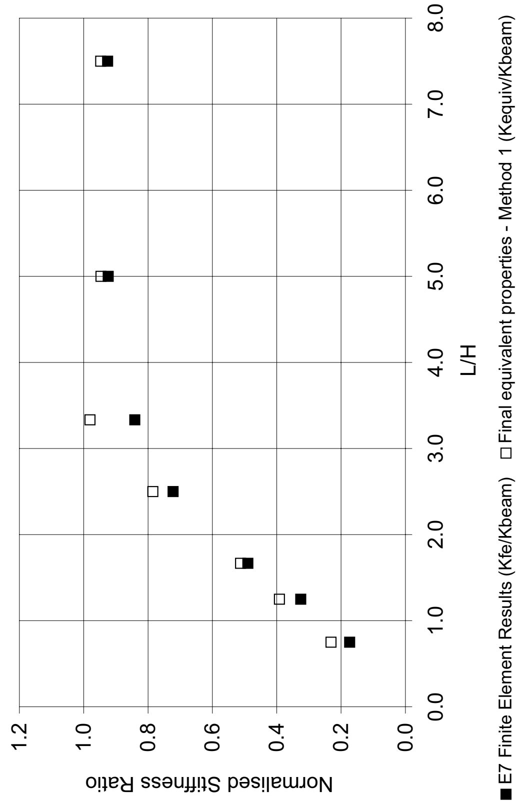

(b) Models E7 - 5.625% Windows

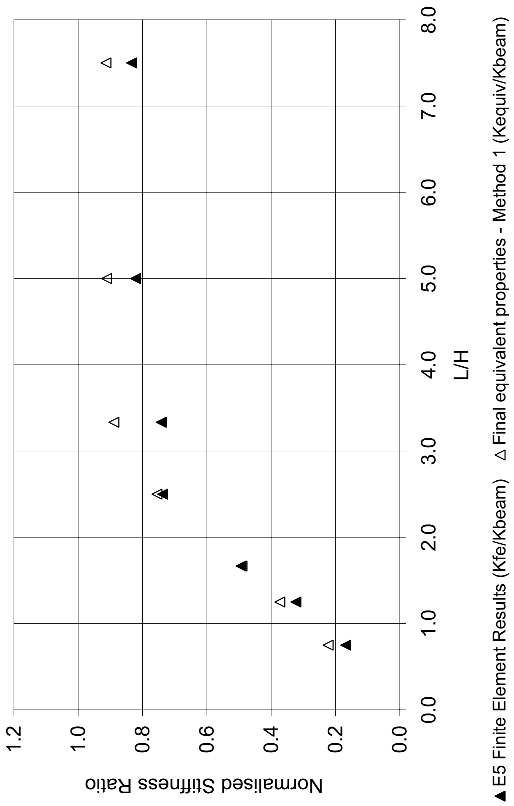

(c) Models E5 - 9.375% Windows

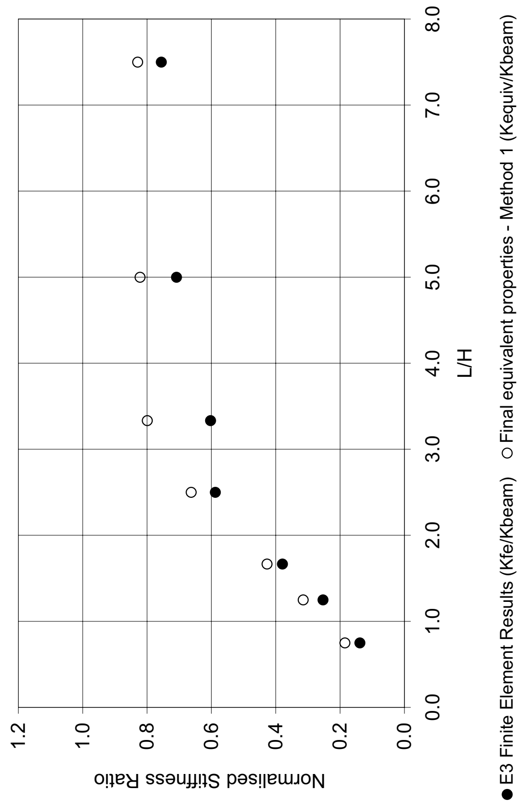

(d) Models E3 - 18.750% Windows

Figure 4.16: **Predicted and observed normalised stiffness ratio - Method 1 (smooth based)**

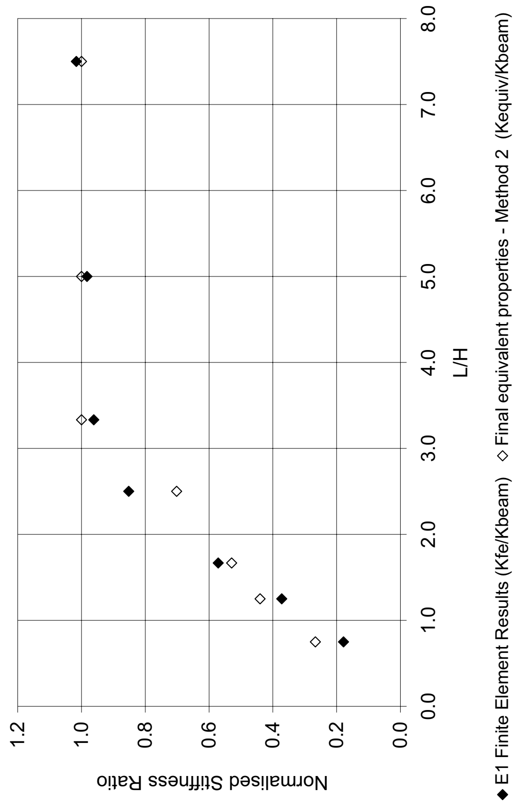

(a) Models E1 - No Windows

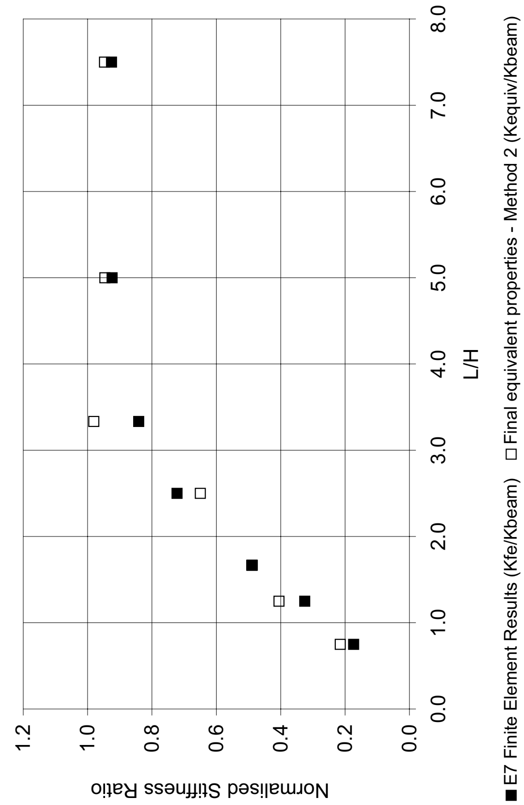

(b) Models E7 - 5.625% Windows

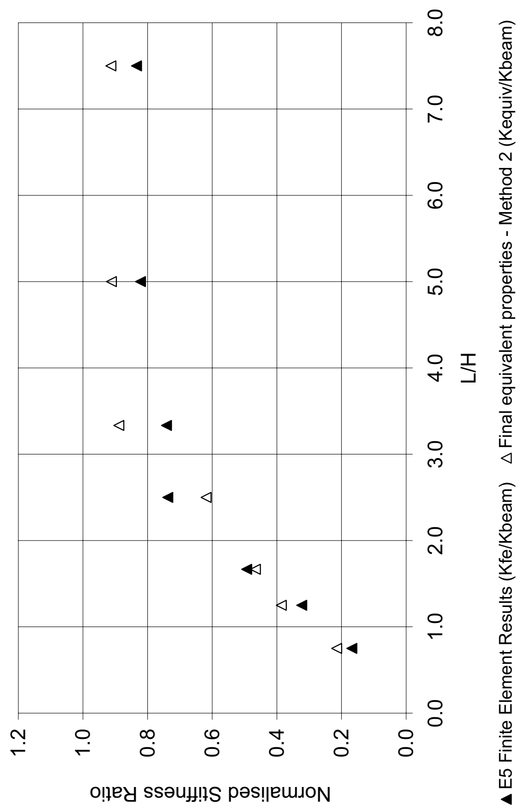

(c) Models E5 - 9.375% Windows

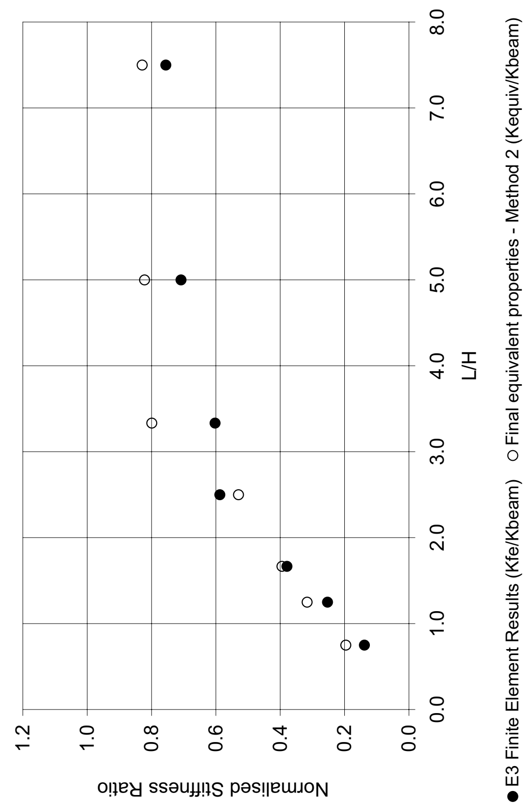

(d) Models E3 - 18.750% Windows

Figure 4.17: **Predicted and observed normalised stiffness ratio - Method 2 (smooth based)**

Chapter 5

Building Facade Analysis - Masonry

5.1 Introduction

This Chapter describes a series of finite element analyses of masonry facades. These analyses are similar to those in Chapter 4 with elastic facades, except that in addition to the impact of facade dimensions, openings and boundary conditions, here a non-linear constitutive model is used to represent masonry brickwork. The full range of facade analyses is summarised in table 4.1 with the masonry analysis schedule in table 5.1. Before the finite element analyses are described, an introduction to the performance of masonry walls and facades subject to ground displacements is given based on a literature review.

5.2 Review of literature

Masonry is a popular building material having historically been extensively used throughout the United Kingdom in the construction of houses, flats and public buildings. The behaviour of masonry as a structural material is more complex, however, than the linear isotropic elastic behaviour that is often assumed in simple analyses. While the assumption of a linear elastic model for masonry may be convenient for simplicity, it is clear that masonry is an inhomogenous material comprising either brick or stone and mortar joints.

Liu (1997) describes typical masonry characteristics including its low tensile strength and propensity to crack under tensile load; anisotropy due to the mortar joints; varying stiffness between the mortar and the blockwork; and the differing behaviour of cracked and uncracked masonry walls. Masonry should thus be modelled using a non-linear approach. Much effort has been devoted to the development of a constitutive model for masonry which captures these characteristics, a number of which are described by Liu (1997).

As discussed in Chapter 2, when surface beams are used to represent a masonry building or facade they are often given linear elastic properties (e.g. Frischmann et al., 1994). It is evident, however, that the approximation of masonry walls and facades by an elastic surface beam may not fully capture the necessary masonry characteristics. A key characteristic overlooked in a linear elastic beam approximation is cracking causing loss of stiffness of the masonry. An attempt to deal with this was introduced in section 2.5.1 in relation to building damage. Burland and Wroth (1974) proposed an approach where a linear elastic response is assumed up to a limiting tensile strain, beyond which the response is not considered. This limiting tensile strain is, however, related to the point at which cracking becomes visible and as Green et al. (1976) note, masonry actually loses its tensile strength at a much lower tensile strain. Green et al. (1976) state that this lower tensile strain is best determined from physical testing.

Burland and Wroth (1974) further note that an important consideration is the mode of deformation of masonry structures; in particular the difference between hogging and sagging. They give examples of walls subjected to angular strains in both hogging and sagging and show that for walls in sagging, where the foundations offer restraint, reasonably uniform distortions occur without significant cracking. For walls in hogging (and thus no restraint at the top tensile face) with the same amount of angular strain, damage is much more severe with significant cracking. Cracking of masonry walls in hogging is shown to be more likely to occur at low deflection ratios (Δ/L) with cracking propagating more rapidly than for walls in sagging, which for the same values of Δ/L sustain little or no damage.

Examples of cracking of masonry model walls in both hogging and sagging are given by Cox (1980) who modelled masonry walls using a friction table. A friction table consists

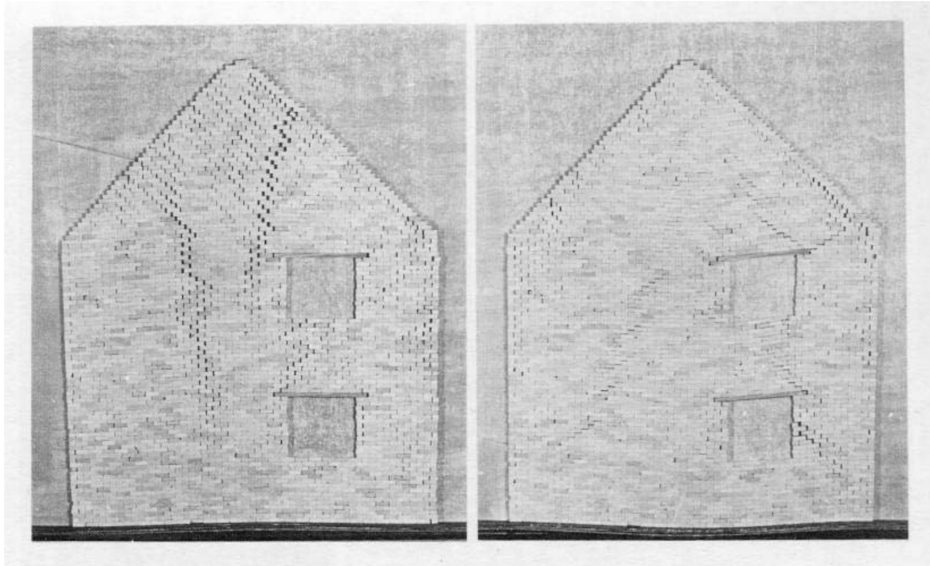

Figure 5.1: **Model masonry facade subjected to hogging (left) and sagging (right) (after Cox, 1980)**

of a table across which a horizontal rough surface slides, much like a treadmill. Walls or building frames can be constructed flat on the rough surface and the movement of the surface from top to bottom of the building simulates gravity. Ground movements at the base of the building are simulated using a beam on which the building rests which can be straight or curved to simulate heave or subsidence. Cox found that in the sagging case, tension cracks were partly suppressed by the restraining action of the 'soil' at the base of the wall and the brickwork 'arching' over the settlement profile and thus supporting itself. In the hogging case, however, little arching was seen as the top of the building is unrestrained and tension cracks were much more severe. Examples of facades subject to ground displacements on the friction table are shown in figure 5.1 in which the greater severity of cracks due to hogging is visible.

Real masonry walls are found to exhibit similar behaviour. In a study of a three-storey, 40m long, 11m wide masonry building subjected to ground movements due to the removal of nearby trees, Cheney and Burford (1974) show sections of external masonry facade subjected to heaving ground (and thus hogging deformation) exhibited wider and progressively worse cracks than other sections of the same building with different deformation modes. Similar observations of the response of a separate four-storey, 75m long, 10m wide brick masonry structure subjected to differential settlement were made by Green et al. (1976)

and these also show that facade sections in hogging were more severely damaged than sections in sagging. The most serious damage occurred in the area of the facade with the worst hogging deformation, where cracks of the order of 10mm wide were observed, whereas in the sagging regions the maximum crack width was 4mm.

More recent ground movements were observed during the tunnelling of the London Underground Jubilee Line Extension (Burland et al., 2001). While these case studies are described in detail in Chapter 9, it is useful to examine briefly the comparative hogging and sagging behaviour of some of the masonry buildings here. The complex including Murdoch, Clegg and Neptune Houses at Moodkee Street, Rotherhithe (described in section 2.6 of this thesis) exhibited some interesting features which differed in hogging and sagging. For Murdoch House, the 40m long northern and southern facades were both in hogging and exhibited flexible responses with the observed base displacements closely following a Gaussian greenfield ground profile. Neptune House, particularly the western facade, exhibited a stiff response over the sagging section with the facade rigidly 'spanning' the expected greenfield trough. The base of the facade, however, followed the greenfield profile (i.e. acted flexibly) in the hogging region (Withers, 2001b). This case study is discussed in detail in Chapter 9 of this thesis.

Finite element analyses also display evidence of masonry facades interacting differently with sagging and hogging ground displacements. During the development and testing of the masonry constitutive model described in section 5.3, Liu (1997) analysed masonry facades subjected to imposed ground displacements. It was observed that once cracked, the masonry walls lost bending stiffness leading to additional strain and thus damage occurring more rapidly than in the uncracked state. A parametric study was also conducted by Liu (1997) using two-dimensional finite element analyses of a masonry building over a tunnel. The stiffness and weight of the masonry facade and its eccentricity over the tunnel were varied. In sagging regions the masonry was observed to form arches. The stress redistribution due to the arching resulted in reduced differential settlement: due to the arches, the pressure on the ground redistributed, with contact pressure in the region of each arch base increasing and the ground pressure remote from an arch base reducing.

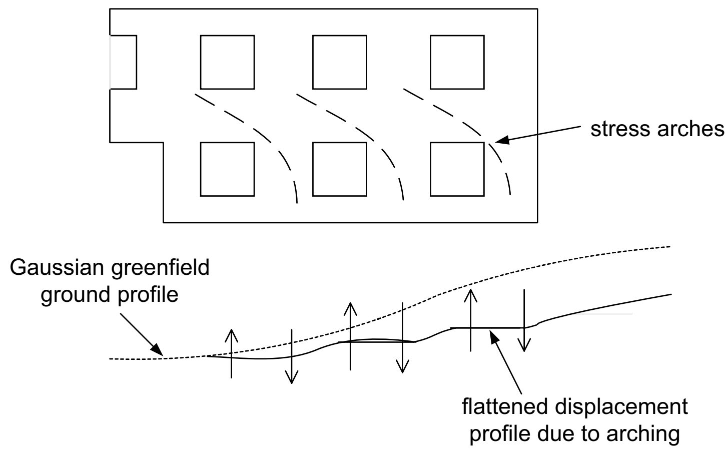

Figure 5.2: **Arching in a masonry facade in sagging (after Liu, 1997)**

This caused soil under the arch bases to settle more than other areas, causing flattening of the settlement trough and the indication of a 'stiff' facade response as shown in figure 5.2. This arching was not observed in facade regions in hogging due to the lack of restraint at the top of the facade and the tensile nature of the horizontal strains in the ground in hogging zones, preventing the formation of stress arches. Liu proposed that the response of a masonry facade could be considered as a beam with supports located at the soil profile inflection points, between which, in the sagging region, the soil profile would be a straight line and outside, in the hogging region, the profile would depend on the facade stiffness.

Boonpichetvong and Rots (2004) present 2D finite element analyses including a masonry facade modelled using a fracture mechanics approach. The facade was placed in the hogging region of tunnelling surface displacements as this was considered the most critical area. The response of the facade indicated that up to a critical level of angular distortion (of 1/800) the facade suffered minimal cracking damage, but beyond this critical level the facade softened and cracks propagated more rapidly. Son and Cording (2005) used a distinct element approach with different properties for masonry bricks and mortar joints in investigating masonry facades adjacent to excavations. They found that the lower the stiffness of the facade, the closer it followed a greenfield surface profile. Crack development was found to further decrease the stiffness of the building and cause the building to more closely follow the greenfield profile.

A number of 3D finite element analyses of tunnels under masonry structures including full soil-structure interaction in 3D, are described by Liu (1997). Augarde (1997) and Burd et al. (2000) also discuss the same analyses (the details of which were described in section 2.5.4). Here, among other observations, it was found that in analyses where the tunnel alignment was oblique under the building, the front facade, which was mostly in sagging, exhibited stress arches leading to flattening of the soil response profile. The front facade thus responded with an almost linear settlement variation from end to end with only minor damage. The rear facade of the structure, however, was predominantly in hogging. No stress arches formed in the rear facade, leaving it with less resistance to the ground displacements and it thus exhibited a much more flexible response. The ground profile under the rear facade followed a profile similar to the greenfield profile with large differential settlements and curvatures. Significant cracking damage was evident at the top of this facade caused by the tensile strains induced by the hogging displacement.

From this review of published literature regarding the performance of masonry walls and facades subject to ground movement it is clear that there is a significant difference in the performance of facades that are subjected to sagging and those that are subjected to hogging deformations. Facades in sagging tend to exhibit arching effects and thus appear to act in a stiff, rigid manner spanning any ground movements, whereas facades in hogging quickly lose stiffness in bending due to the propagation of cracks caused by tensile strains and tend to act in a more flexible manner with the facade base following any ground movements without affecting them. Surface beams designed to represent a masonry facade should therefore also reflect this difference in hogging and sagging response.

5.3 Description of masonry finite element analyses

5.3.1 Introduction

This section describes finite element analyses of masonry facades undertaken using a similar approach to the analyses of linear elastic facades described in section 4.2.4 of this thesis. Two-dimensional facades are subjected to an applied ground displacement and their response is investigated with a view to developing a simple non-linear surface beam model to represent masonry facades that responds appropriately in hogging and sagging for use in finite element analyses of tunnelling.

5.3.2 Meshes

The meshes used in the analyses are identical to those used for the elastic analyses described in Chapter 4. The full range of masonry facades analysed is given in table 5.1 with the key variables of facade dimensions and proportion of openings. Masonry facades are identified using a similar scheme to the elastic facades in table 4.2 with the reference 'M' used to indicate that the constitutive model is a non-linear masonry model. The facade meshes are shown in Appendix A.

5.3.3 Masonry material model

The constitutive model used to represent the masonry is an elastic no tension model developed by Liu (1997) in which material under compression behaves elastically, while material in tension will crack where tensile stress develops, after which stiffness in a direction perpendicular to the crack reduces to a small value. The approach taken is a macroscopic one to modelling masonry where the material is treated as a continuum and the properties of the bricks and the mortar are averaged rather than accounted for separately as they would be in a microscopic approach (which is computationally more expensive). Additionally, a smeared cracking approach is adopted where the cracked masonry is assumed to remain as a continuum as opposed to cracks being considered individually. Liu (1997) includes three states in the constitutive model: elastic intact, single cracked and double cracked; each of which has its own stiffness matrix as described below. The model is implemented in the OXFEM finite element program where the modified Euler solution scheme is used to deal with the non-linearity of the material (Burd, 1986). Further details about the solution techniques in OXFEM can be found in section 7.5.

Table 5.1: **Schedule of facade meshes for masonry analyses**

Facade Family	Facade Number	Length (m)	Height (m)	L/H Ratio	Openings (%)
M1	M11	60	8	7.50	0
M1	M12	40	8	5.00	0
M1	M13	20	8	2.50	0
M1	M14	40	12	3.33	0
M1	M15	20	12	1.67	0
M1	M16	20	16	1.25	0
M1	M17	12	16	0.75	0
M3	M31	60	8	7.50	18.750
M3	M32	40	8	5.00	18.750
M3	M33	20	8	2.50	18.750
M3	M34	40	12	3.33	18.750
M3	M35	20	12	1.67	18.750
M3	M36	20	16	1.25	18.750
M3	M37	12	16	0.75	18.750
M5	M51	60	8	7.50	9.375
M5	M52	40	8	5.00	9.375
M5	M53	20	8	2.50	9.375
M5	M54	40	12	3.33	10.000
M5	M55	20	12	1.67	10.000
M5	M56	20	16	1.25	9.375
M5	M57	12	16	0.75	9.375
M7	M71	60	8	7.50	5.625
M7	M72	40	8	5.00	5.625
M7	M73	20	8	2.50	5.625
M7	M74	40	12	3.33	6.250
M7	M75	20	12	1.67	6.250
M7	M76	20	16	1.25	5.625
M7	M77	12	16	0.75	6.250

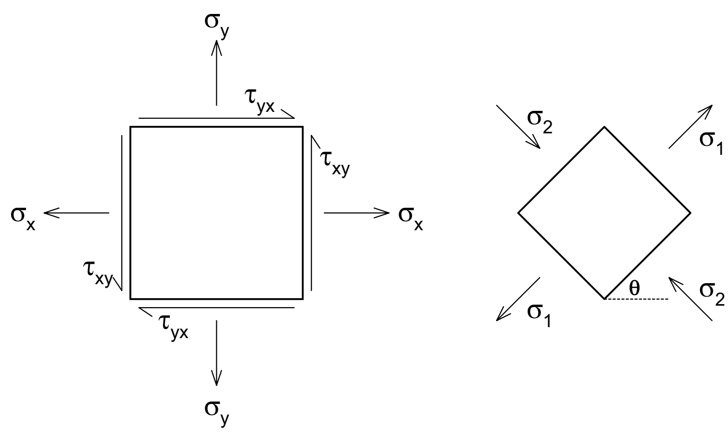

Figure 5.3: **Elastic no-tension model principal stresses (after Liu, 1997)**

The stresses on a masonry element are shown in figure 5.3. For these stresses σ_x, σ_y and τ_{xy}, the incremental stress and strain are related by the tangent stiffness matrix $\boldsymbol{D}$ by

$$d\sigma = \boldsymbol{D} d\epsilon \tag{5.1}$$

If both principal stresses, σ_1 and σ_2, are compressive then the material is elastic and the incremental stiffness is given by

$$\boldsymbol{D} = \frac{E}{1-\nu^2} \begin{pmatrix} 1 & \nu & 0 \\ \nu & 1 & 0 \\ 0 & 0 & \frac{1-\nu}{2} \end{pmatrix} \tag{5.2}$$

If major principal stress σ_1 is tensile while σ_2 is compressive, the material is singly cracked in a direction perpendicular to the major principal stress giving an incremental stiffness in the principal stress space of

$$\boldsymbol{D'} = \begin{pmatrix} 0 & 0 & 0 \\ 0 & E & 0 \\ 0 & 0 & 0 \end{pmatrix} \tag{5.3}$$

which can be multiplied by a transformation matrix using θ to give $\boldsymbol{D}$ in x-y coordinate space where θ is the inclination of the principal strain direction, taking compression as

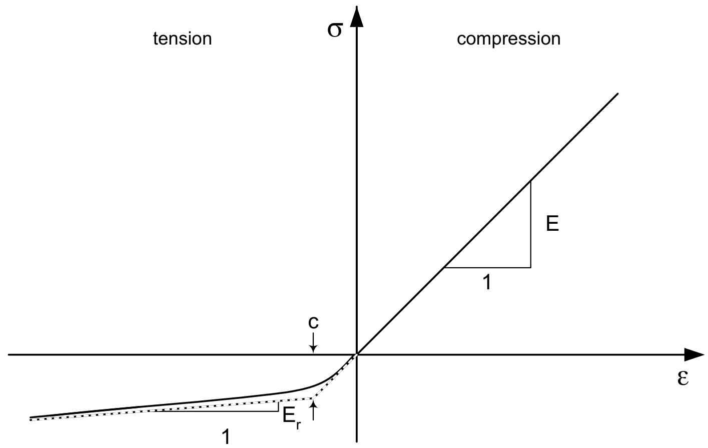

Figure 5.4: **Elastic no-tension masonry constitutive model (after Liu, 1997)**

positive. If both σ_1 and σ_2 are tensile, the material is doubly cracked and the incremental stiffness is set to a small residual value, E_r.

The material in the model is given an infinite compressive strength and a low tensile strength as shown in figure 5.4. The material is considered cracked when the tensile stress reaches a critical value, c, as shown. A residual stiffness for the material is required for numerical stability and to avoid a multitude of unrealistic minuscule cracks appearing (Liu, 1997). The residual stiffness, E_r, is calculated using a residual stiffness factor f as

$$E_r = f \times E \tag{5.4}$$

In addition, the stiffness is reduced gradually as tensile stress develops to avoid problems associated with crack re-closure as described by Liu (1997). A stiffness reduction rate parameter ϵ_o^{cr} controls the speed at which the stiffness decreases. The notion of cracking strain, ϵ^{cr} was introduced by Liu to monitor the cracking process and any reclosing during stress and state updating. This was necessary as stress normal to a cracking direction is ideally zero after cracking.

Elastic lintels above the windows in the mesh were used to avoid failure of the masonry above the openings. This not only avoids complications associated with material failure but replicates the common situation found in real masonry buildings, where lintels are used. Over-integration with 16 Gauss points is used during solution to smooth the integration

Table 5.2: **Material properties for no-tension masonry model**

E	ν	γ	f	c	ϵ_o^{cr}
1.0×10^7kPa	0.2	20kPa/m	0.01	10kPa	$4\mu\epsilon$

Table 5.3: **Material properties for elastic lintels**

E	ν	γ
1.0×10^7kPa	0.2	20kPa/m

due to the non-linear nature of the material.

The properties of the non-linear masonry and elastic lintel materials are given in table 5.2 and table 5.3 where: E is Young's Modulus in compression, ν is Poisson's ratio, γ is self weight, f is the residual stiffness factor, c is the residual tensile strength, and ϵ_o^{cr} is the stiffness reduction ratio.

5.3.4 Displacement and boundary conditions

For each facade analysis, displacements are imposed at base level and the response is analysed. These imposed displacements are the same form as the those applied for the elastic facade analyses of section 4.2.4 and given by equation 4.5. The magnitude of the displacements applied for the masonry analyses, however, is different to those for the elastic analyses. Appropriate magnitudes of displacement for each facade were found by using the damage category chart of Boscardin and Cording (1989) and the interaction charts for deflection ratio (Δ/L) based on the one presented by Burland (1997), as described below.

For the case of a facade with $L/H = 1.0$, Burland used the limiting strain values (ϵ_{lim}) proposed by Boscardin and Cording (1989) (and given as table 2.2 in this thesis), to produce the interaction chart in figure 2.8; using the equations presented as 2.17 to 2.21 in this thesis to do so. From this chart, making the assumption that horizontal strain at the ground surface (ϵ_h) is zero (i.e. there is only bending and shear strains present, not additional ground induced horizontal strains), values of Δ/L can be read off for a chosen damage category. From the midpoint displacement (Δ) so found, equation 4.5 is used to

Table 5.4: **Maximum central displacement for masonry facades**

Facade Number	**MX1**		**MX2**		**MX3**		**MX4**		**MX5**		**MX6**		**MX7**	
Lower Boundary	r	s	r	s	r	s	r	s	r	s	r	s	r	s
Displacement (mm)	72	121	41	58	20	23	44	41	28	20	31	22	18	18

calculate the corresponding value of w_o which is then used to determine the displacement to apply at all nodes along the base of the facade, again using equation 4.5.

For this series of analyses the appropriate final level of damage for the masonry facades was chosen as category two (slight) damage. To determine the deflection ratio (Δ/L) to apply to each facade to achieve this damage, interaction charts for each value of L/H for the masonry facades given in table 5.1 were produced (using the same approach as Burland (1997)) and examples are given in figure 5.5. From these charts, values of Δ/L were read off for $\epsilon_h = 0$ at the upper boundary of damage category two. The maximum resulting displacement at the centre of each of the various facade shapes is given in table 5.4 for hogging ('MX1' represents the value for facades M11, M31, M51 and M71); sagging displacements are similar but negative.

As with the elastic facades, two boundary conditions were used in the analyses, a smooth (s) base where the base of the facade is free to move horizontally and a rough (r) base where horizontal movement is restrained. Displacements causing both hogging (h) and sagging (s) were imposed on each facade with each boundary condition.

5.3.5 Calculation procedure

Each analysis is conducted in two stages. In the first stage, the facade self weight is applied. Displacements and strains are then reset to zero and in the second stage, the imposed ground displacements are applied. Facade strains and crack damage is thus solely a result of the applied ground displacements. To consider the response of the facade as the displacements develop, the total displacement y_t at each node is divided by the number of steps in the stage, n, and a value of y_t/n is applied at each step. Thirty steps are used for these facade analyses with results output at steps one, three, five, 10, 20 and 30.

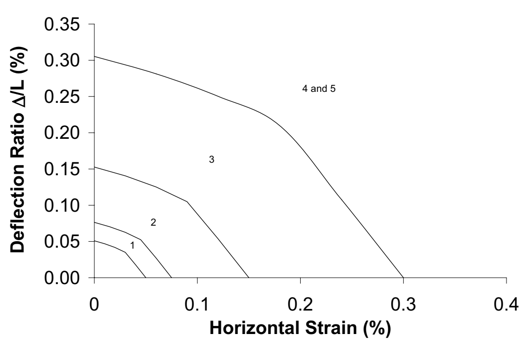

(a) L/H = 0.75

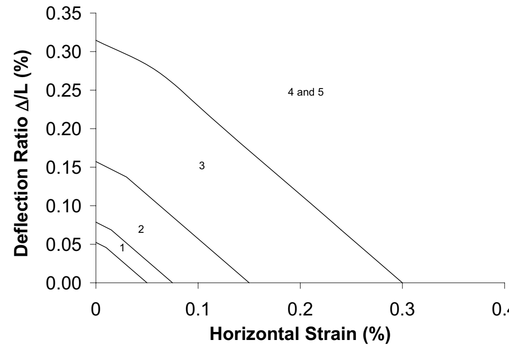

(b) L/H = 1.25

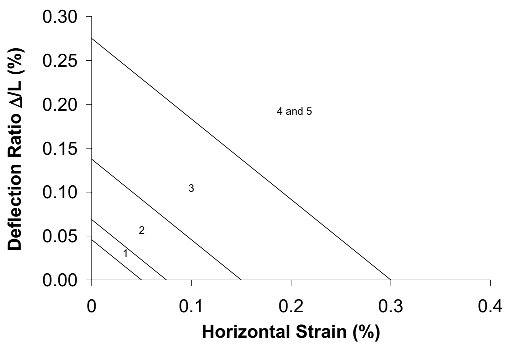

(c) L/H = 1.67

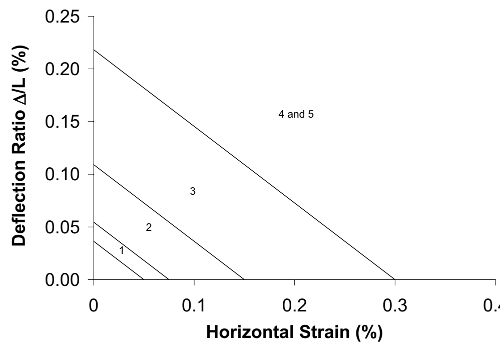

(d) L/H = 2.50

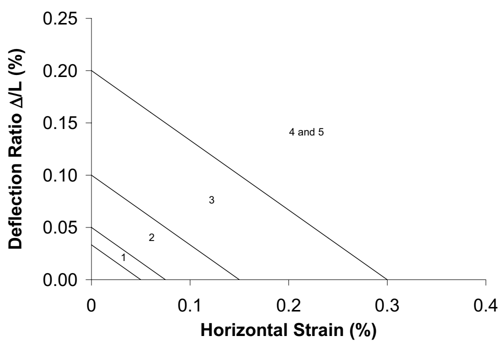

(e) L/H = 3.33

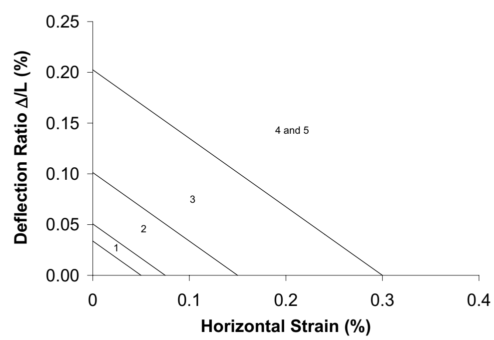

(f) L/H = 5.00

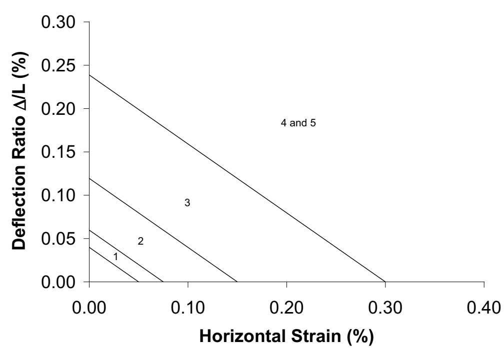

(g) L/H = 7.50

Figure 5.5: **Interaction charts for deflection ratio and horizontal strain showing damage categories (assuming a rough base boundary condition)**

5.3.6 Results

Presentation of finite element results

Results for the elastic analyses presented in section 4.2.6 of this thesis are based on the stress at the base of the facades. For the masonry facade analyses in this section, however, this approach to presenting the results is not appropriate. It is not possible to infer the reaction of the full facade from the reaction at the base as it is in an elastic facade, due to the non-linear nature of the masonry constitutive material used and its ability to crack. The stress at a facade base is still a useful result to investigate but in order to gain a full understanding of the reaction of the facades to the imposed displacements, contour plots of stress and strain, crack patterns and damage over the whole facade are required.

Cracking strain, ϵ^{cr}, is used to describe the damage to the masonry structures due to the ground displacements, following the approach of Liu (1997). Total strain can be considered as comprising two parts, the elastic strain, ϵ^{e}, and the cracking strain, ϵ^{cr} as follows

$$\epsilon^{total} = \epsilon^{e} + \epsilon^{cr} \tag{5.5}$$

Liu (1997) concluded that is is reasonable to use the cracking strain (excluding the elastic part of the deformation) rather than the total strain to describe the severity of damage to masonry facades. Cracking strain can be resolved into three components: ϵ_1^{cr} representing the component normal to the initial crack; ϵ_2^{cr} representing the component normal to any second crack; and γ_{12}^{cr} representing the shear deformation across the crack (Liu, 1997). This approach differs from that of Boscardin and Cording (1989) who use total tensile strain in their correlated damage grades. The cracking strain approach was, however, found by Liu (1997) and Burd et al. (2000) to be a reasonable approach for masonry structures and as such, damage grades based on cracking strain are presented here.

Crack patterns can also be predicted from the finite element results and are presented by drawing short lines on the facade in the direction of the expected crack for points at which the crack strain exceeds $500\mu\epsilon$. The density of the lines indicates the severity of cracking;

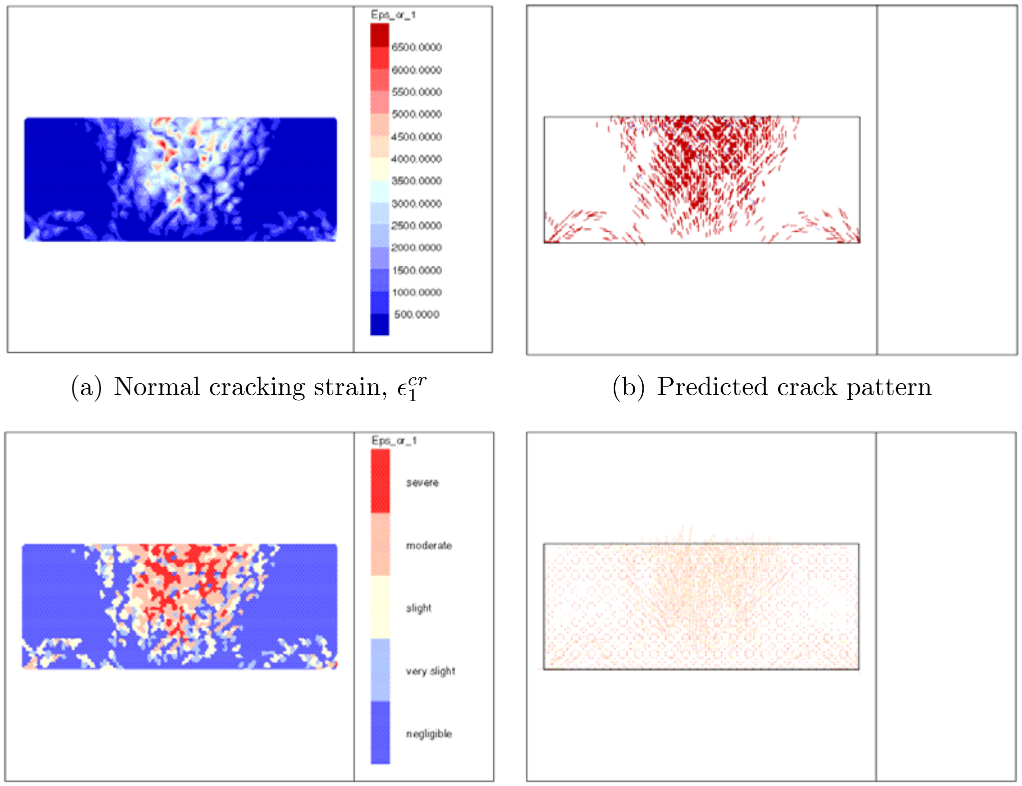

(a) Normal cracking strain, ϵ_1^{cr}

(b) Predicted crack pattern

(c) Damage category

(d) Stress trajectory

Figure 5.6: **M13rh Rough/Hogging**

a double thick line is drawn when strain exceeds $1000\mu\epsilon$ and a triple line when it exceeds $1500\mu\epsilon$.

Effects of hogging and sagging boundary conditions

Results for analysis M13 are presented for imposed hogging (h) and sagging (s) displacements for both rough (r) and smooth (s) boundary conditions. For each of these cases results are presented for normal cracking strain (ϵ_1^{cr}), crack pattern, damage grade and stress trajectory at the final calculation step (30). Results are shown in figures 5.6 to 5.9.

Facades in hogging are seen to crack vertically for almost their full height in the centre, with cracking and damage concentrated at the top of the facade in the areas of high strain, as can be expected due to the unrestrained nature of movement at this boundary. Damage is also evident at the bottom corners of the hogging facades where shear strains also develop. The hogging facade with the rough boundary condition can be seen to sustain more serious

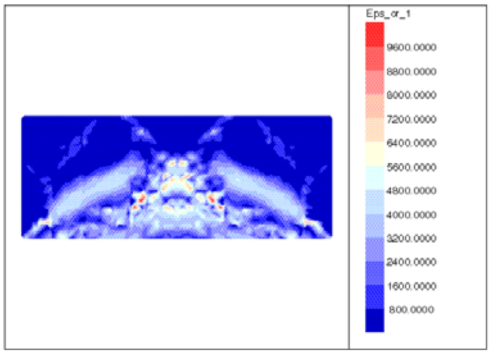

(a) Normal cracking strain, ϵ_1^{cr}

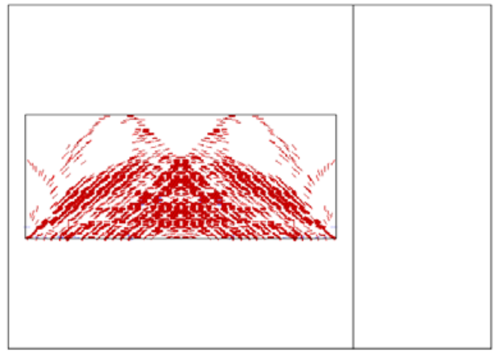

(b) Predicted crack pattern

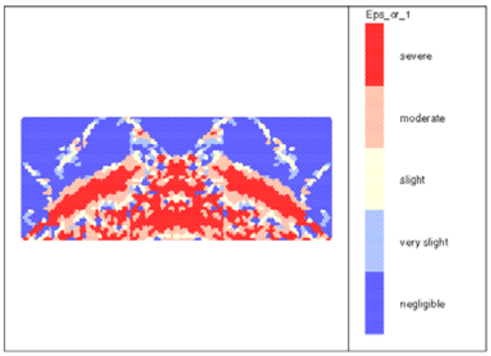

(c) Damage category

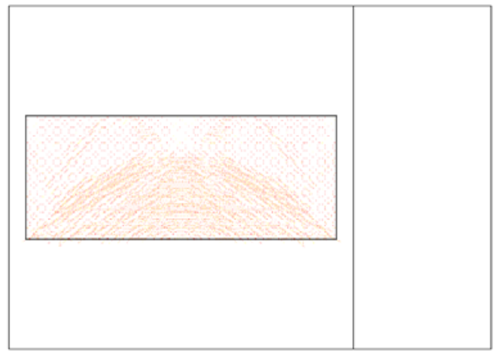

(d) Stress trajectory

Figure 5.7: **M13rs Rough/Sagging**

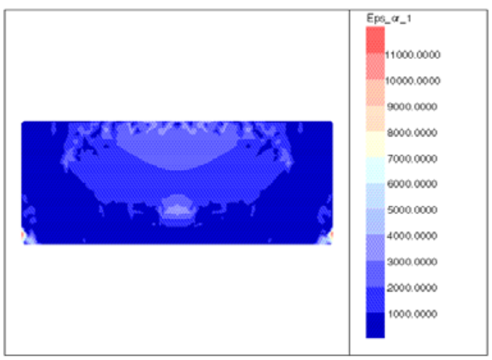

(a) Normal cracking strain, ϵ_1^{cr}

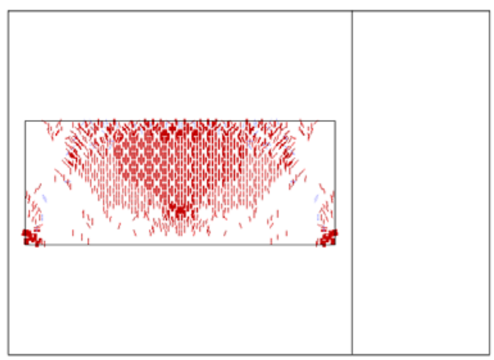

(b) Predicted crack pattern

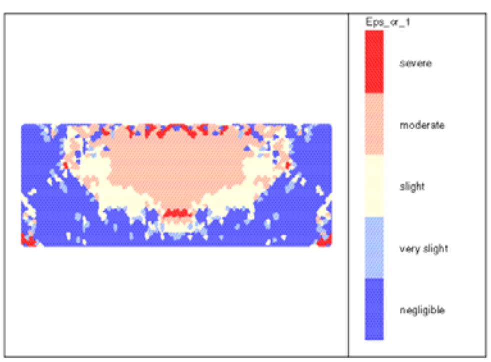

(c) Damage category

(d) Stress trajectory

Figure 5.8: **M13sh Smooth/Hogging**

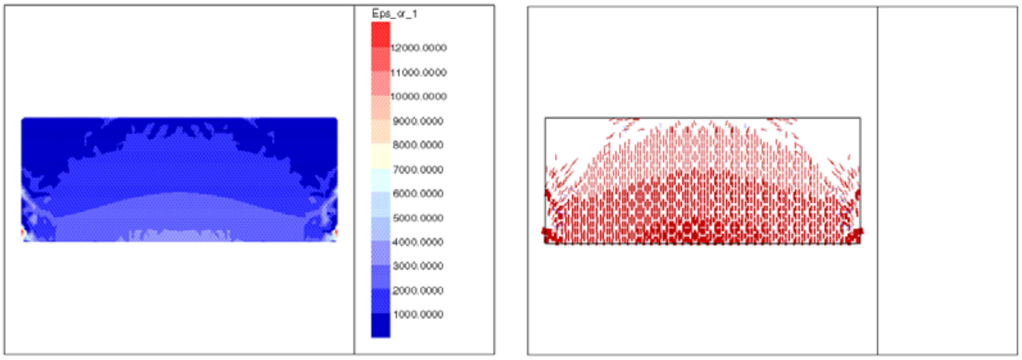

(a) Normal cracking strain, ϵ_1^{cr} (b) Predicted crack pattern

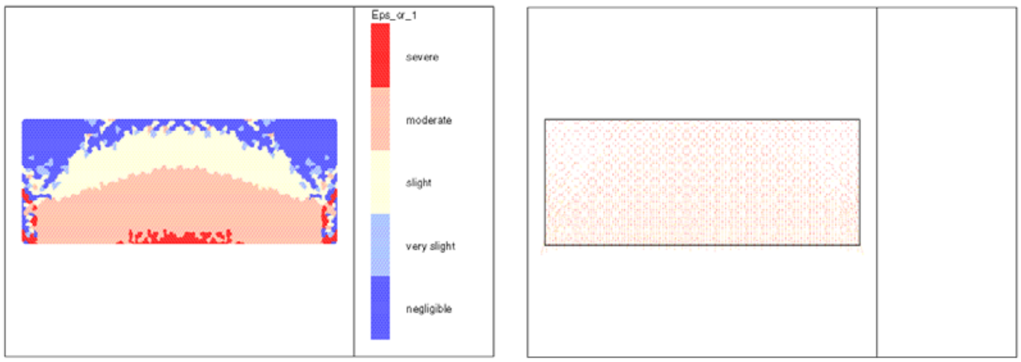

(c) Damage category (d) Stress trajectory

Figure 5.9: **M13ss Smooth/Sagging**

damage than that with the smooth boundary condition. This is possibly due to the rough boundary forcing the neutral axis to lie at the ground surface of the rough based facade. The amount of *moderate* and *severe* damage overall is higher than expected given the choice of applied displacement magnitude discussed above. This is possibly due to the non-linear nature of the masonry material and the use of the cracking strain to determine the grades, as opposed to the elastic theory (and total strain values) upon which the damage grades were originally developed. Cracks in the hogging facades are mostly vertical indicating that they are mainly bending related rather than shear induced, although there are some diagonal shear cracks in areas of high shear strain near the supports.

Sagging facades can be seen to exhibit the predicted stress arching (most evident from the stress trajectory plots), with significant crack damage occurring under the arch, but very little above it due to the arch's supporting action. This is more pronounced in the rough based facade which has a more clearly defined arch under which mainly diagonal and some horizontal cracking appears, indicating vertical downwards movement of the facade material. Arching in the smooth facade is much less pronounced due to the lack of horizontal support for potential arch foundations at the base. Cracking here is mostly vertical indicating spreading of the facade horizontally at the unrestrained lower boundary. No significant arching is evident in the facades in hogging except for the lower corners of the rough based facade. Here small arches are evident due to the shape of the applied displacement profile at this position, where a small sagging zone exists.

The changing response of the facade as the imposed displacement increases is shown in figure 5.10. Here the maximum central displacement is plotted against average vertical force at each node along the facade base as the calculation progresses. Data are plotted at calculation steps one, three, five, 10, 20 and 30. For both hogging and sagging after a certain number of steps, the relationship becomes a straight horizontal line indicating the overall incremental stiffness of the facade is zero (i.e. no more force is generated as the displacements increase). The force lines appear to tend towards a value of 80N which again indicates that the facade weight is the only contributor to this contact force, as the nodes are at intervals every half metre (and the weight is 160N/m). The slight differences in the sagging forces are thought to be due to differing arch shapes in the smooth and rough case. The loss of stiffness appears to occur by calculation step 10 (smooth: Δ/L=0.038%, rough: Δ/L=0.033%).

Figure 5.11 shows the development of cracks as the displacement increases. The hogging facade can be seen to be cracked almost to its full height by step 10 (Δ/L=0.033%) and the arch in the sagging case can also be observed due to the cracking occurring underneath. These observations confirm the response indicated in figure 5.10.

For facades in hogging, ground heave thus appears able to occur unrestrained once cracking of the facade reduces the effective flexural rigidity to zero, due to the lack of restraint at the top of the facade meaning that arching can not occur. Facades in sagging, although cracking also occurs (possibly to a greater extent), exhibit an action where the facade is supported by the arch. This arching action allows the masonry facade to ‘span’ sagging displacements as if it was a stiff beam. These observations hold for both boundary conditions, rough and smooth and concur with the observations in the literature.

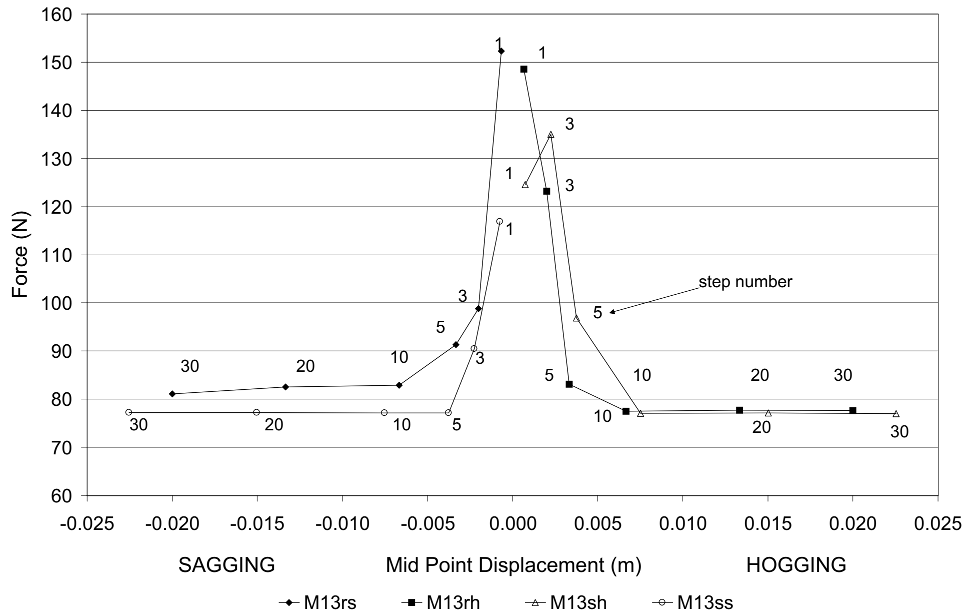

Figure 5.10: **Force displacement relationship at facade base**

To investigate the impact of the other factors found to be critical in the elastic facade analysis, the overall facade dimensions and the amount of openings in the facade, further results are discussed below.

It is apparent from the results presented above that similar effects are evident for facades with both rough and smooth base conditions (although those facades with rough bases appear to suffer more damage) and thus similar conclusions can be drawn about facade response from analyses with either base condition. Contour plots for facades with rough bases only are therefore presented in the remaining sections.

Effect of increasing amounts of openings

Results are presented in this section for facades M33 (18.750% windows), M53 (9.375% windows) and M73 (5.625% windows). These facades have the same overall dimensions (20m x 8m) as facade M13 discussed above. The various plots given in figures 5.12 and 5.13 are for the final analysis step (step 30, Δ/L=0.100%)

Facades with openings exhibit similar key characteristics to those without openings: facades in sagging can again be seen to exhibit arching, whereas those in hogging do not. An effect

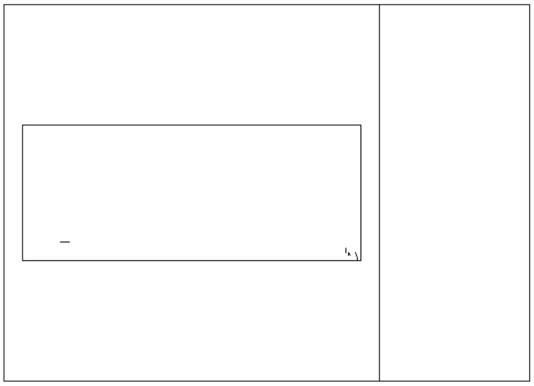

(a) M13 Hogging crack pattern: Δ/L=0.010%

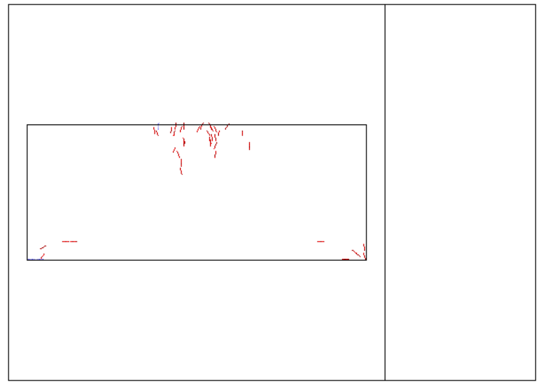

(b) M13 Hogging crack pattern: Δ/L=0.017%

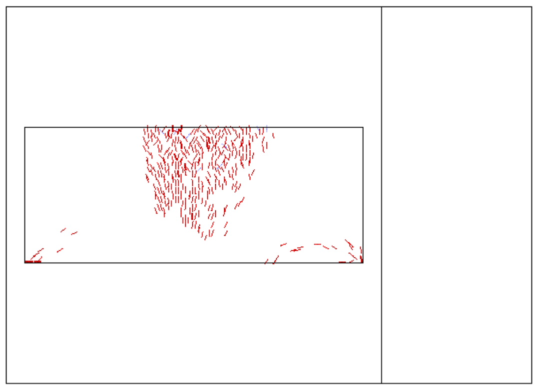

(c) M13 Hogging crack pattern: Δ/L=0.033%

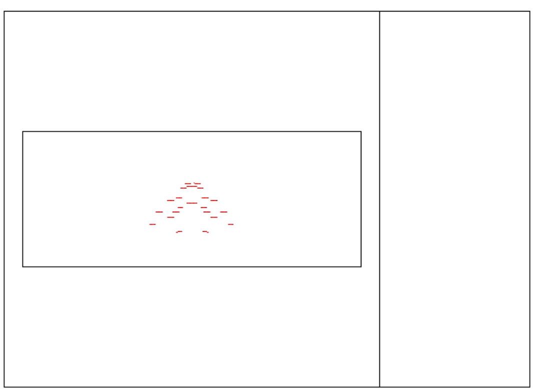

(d) M13 Sagging crack pattern: Δ/L=0.010%

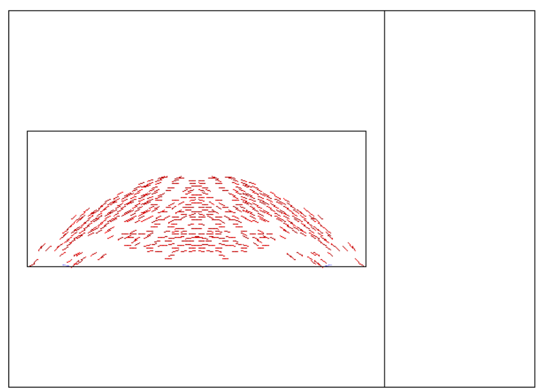

(e) M13 Sagging crack pattern: Δ/L=0.017%

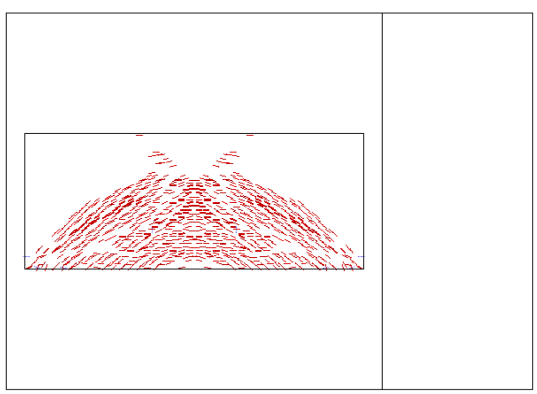

(f) M13 Sagging crack pattern: Δ/L=0.033%

Figure 5.11: **Development of cracks in masonry facades with rough bases**

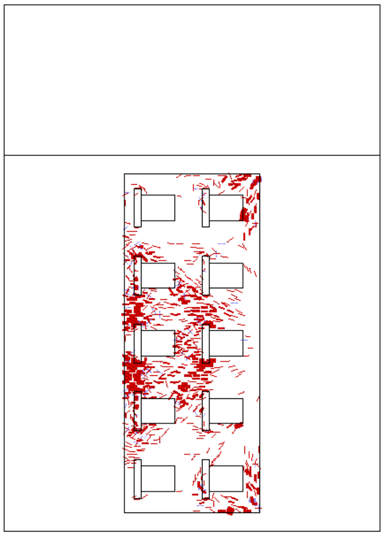

(a) M33 Crack pattern

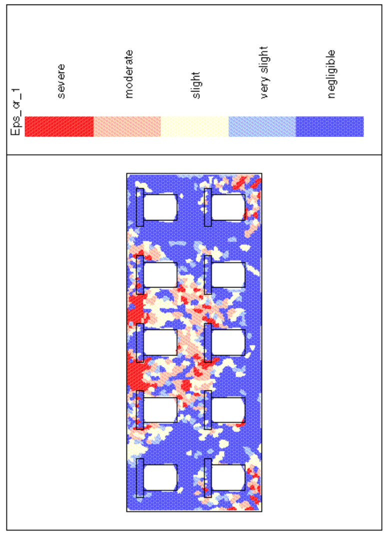

(b) M33 Damage category

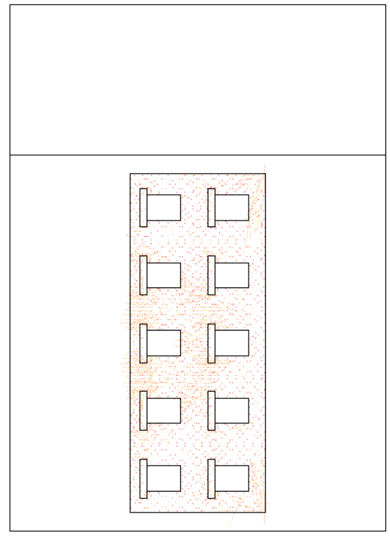

(c) M33 Stress trajectory

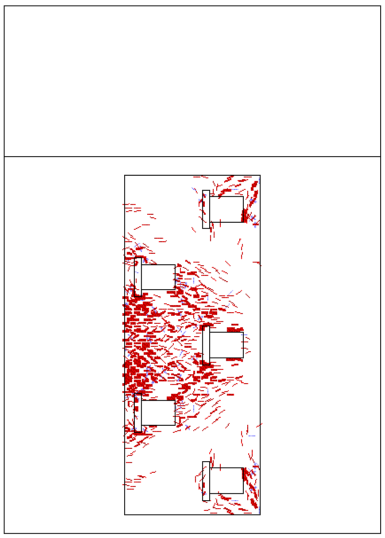

(d) M53 Crack pattern

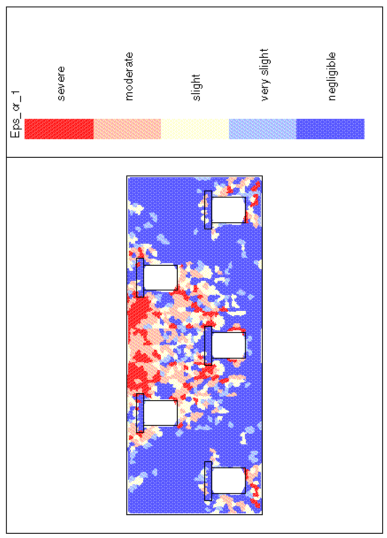

(e) M53 Damage category

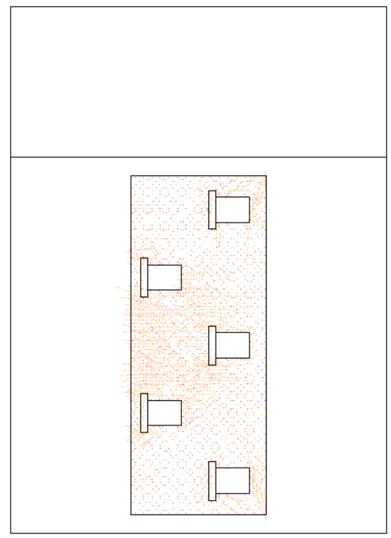

(f) M53 Stress trajectory

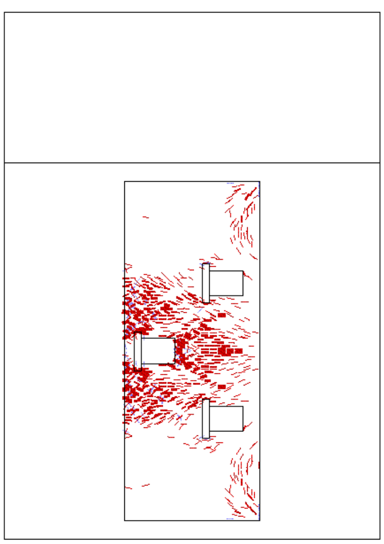

(g) M73 Crack pattern

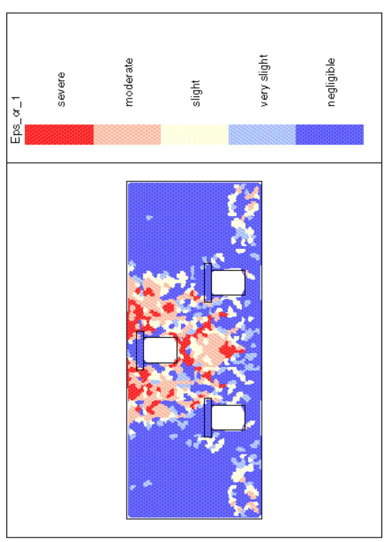

(h) M73 Damage category

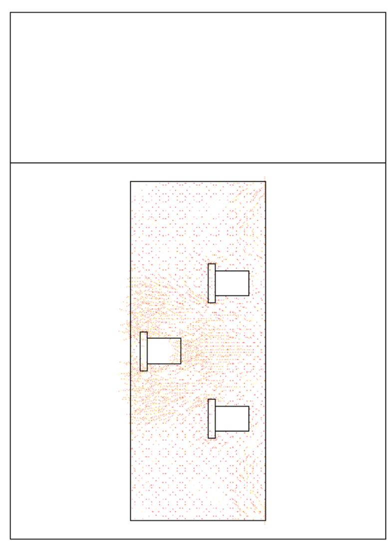

(i) M73 Stress trajectory

Figure 5.12: **Effect of openings - Rough/Hogging**

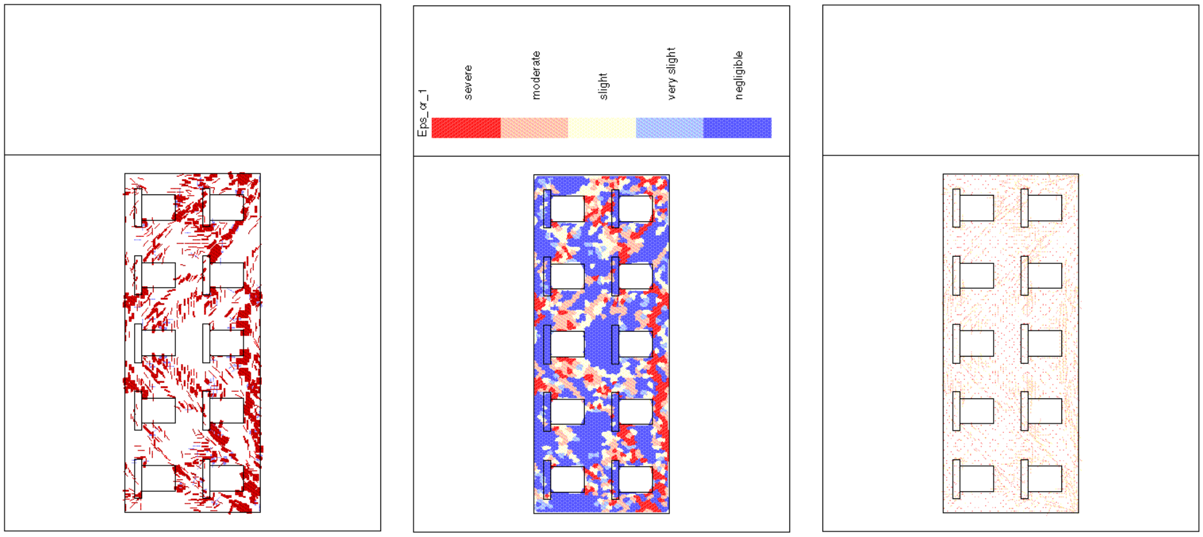

(a) M33 Crack pattern (b) M33 Damage category (c) M33 Stress trajectory

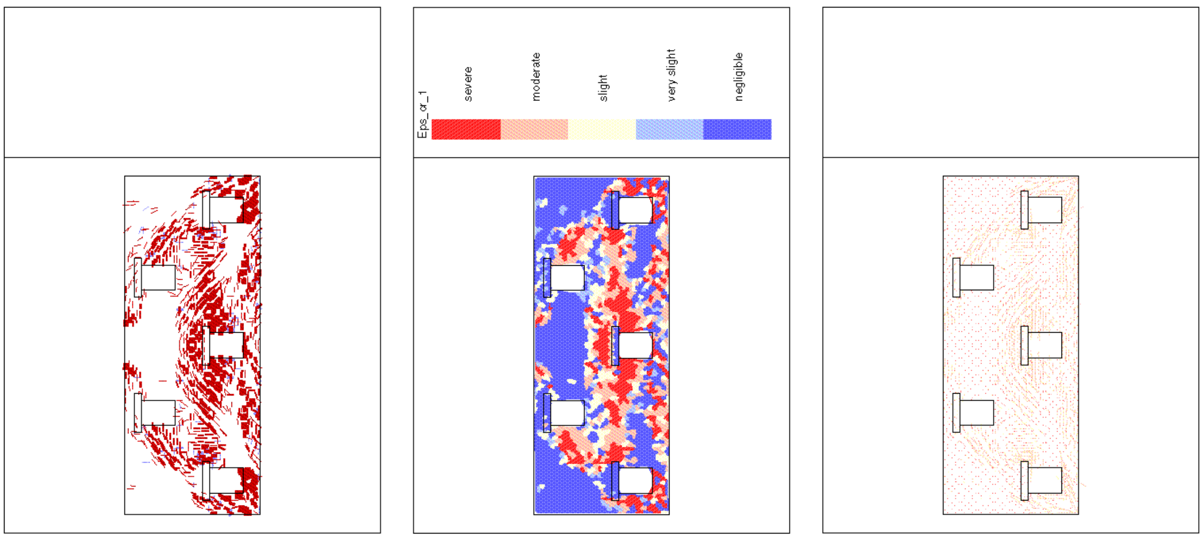

(d) M53 Crack pattern (e) M53 Damage category (f) M53 Stress trajectory

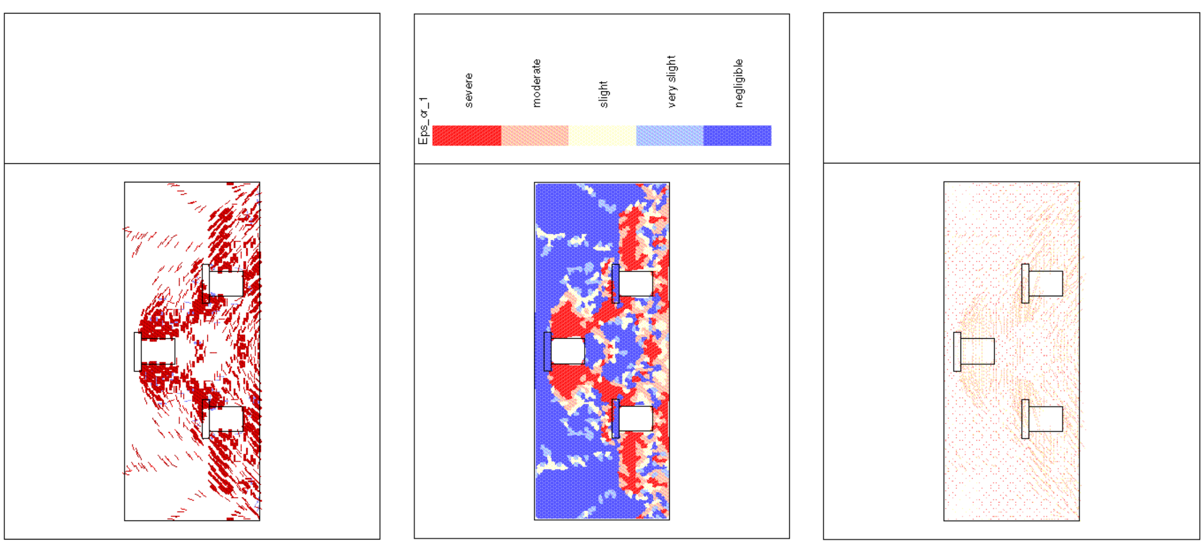

(g) M73 Crack pattern (h) M73 Damage category (i) M73 Stress trajectory

Figure 5.13: **Effect of openings - Rough/Sagging**

of adding openings to the facades can be clearly seen in the concentrations of crack damage at the corners of the windows which lead to additional damage. Damage can also be seen to be spread over greater areas of the facade, the higher the number of openings. The stress arching in the sagging facades also differs slightly due to openings in the facades, as the stress arches must find their way around the windows and doors. Two stress arches, rather than one, develop in facades M53 and M33 in sagging (figure 5.13) due to the pattern of windows. The additional damage due to this occurrence is particularly evident in facade M33 where significant damage can be seen around windows close to the lower corners of the facade as the stress arches attempt to reach the base.

To determine if the addition of windows has any effect on the rate at which the facades crack sufficiently to lose their overall stiffness, figure 5.14 showing the average nodal force along the base as the displacement is applied (similar to figure 5.10). For all facades, irrespective of the amount of openings, the direction of imposed displacement (or indeed the boundary condition), the cracked state, evidenced by horizontal force plots, is reached by step 10 (smooth: Δ/L=0.038%, rough: Δ/L=0.033%). Hogging facades can be seen to all reach a force representing the self weight of the facade consistently for both rough and smooth boundary cases (the differing self weights being due to the differing amounts of openings). Sagging facades, however, exhibit different force values near the weight of the facade, but not all agreeing exactly. This is thought to be due to the amount of the facade weight supported by the different arch effects within individual facades.

Increasing the amount of openings appears to have little effect on the general nature of the facade response or the maximum damage grade, although crack patterns and damage grade differ due to window layouts and there exists localised damage around window corners. Increasing the amounts of windows does not appear to affect when the facade loses its stiffness. Sagging facades again experience arching which is absent in hogging.

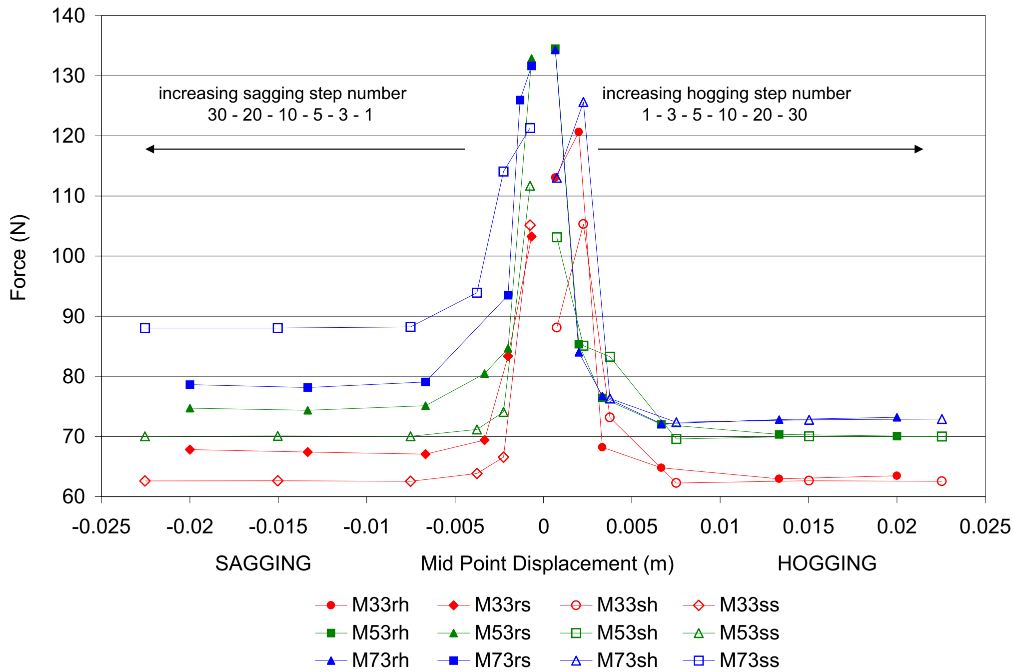

Figure 5.14: **Force displacement relationship at facade base - Differing % windows**

Effect of differing overall geometry

The response of facades with differing overall dimensions (L/H) were analysed for the M1 family with no windows (facades M11, M12, M14, M15, M16 and M17) for hogging and sagging. Figure 5.15 shows plots for facade M16 for the final calculation step (step 30). Other facades were analysed but are not shown here.

As would be expected, despite the differing overall dimensions of the facades, those in

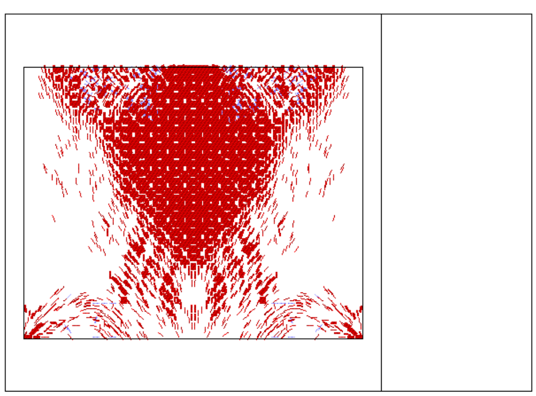

(a) M16 Crack pattern: Rough/Hogging

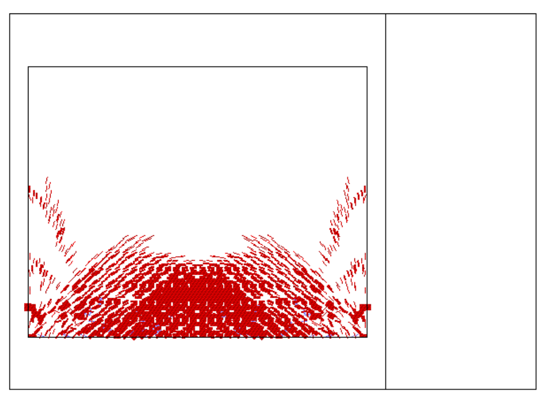

(b) M16 Crack pattern: Rough/Sagging

Figure 5.15: **Cracking plots for facade M16**

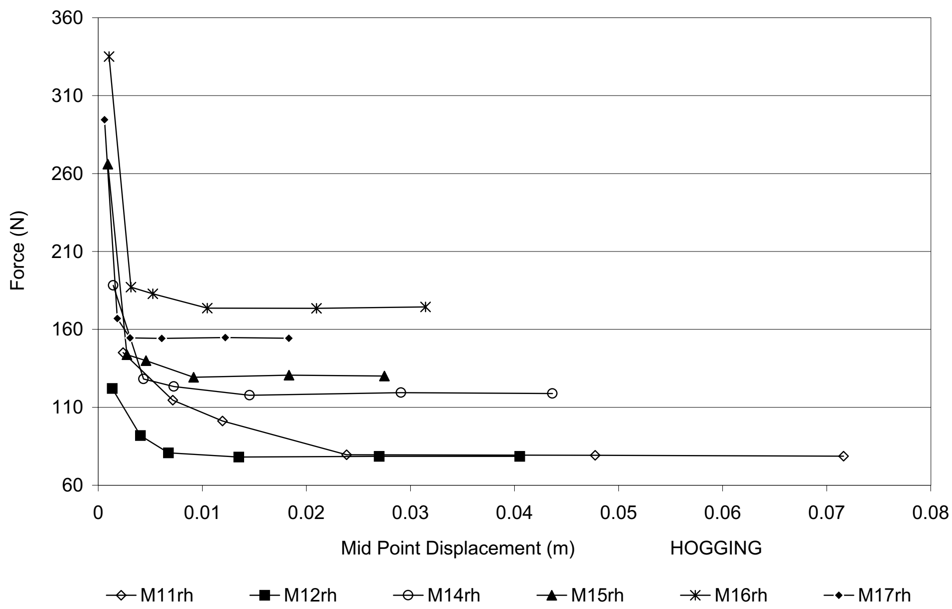

Figure 5.16: **Force displacement relationship at facade base - Differing L/H**

sagging exhibited arching, whereas those in hogging did not. One notable feature of the facades with low values of L/H is that the damage is confined to the lower portion of the facade in the sagging case. This echoes comments made earlier in section 4.3.2 about facades potentially having a 'limiting height' above which they are not affected by ground movements. This can be seen in figure 5.15 only to be true in sagging and is due to the arching effect whereby material above the arch is supported and not damaged by the ground movements.

Figure 5.16 shows the average nodal force (for the rough hogging case only for clarity) along the base as the displacement is applied to this family of windowless facades. The cracked state (again, shown by the response flattening to a horizontal line) is reached by all facades by step 10 (M11: Δ/L=0.040%, M12: Δ/L=0.034%, M14: Δ/L=0.036%, M15: Δ/L=0.046%, M16: Δ/L=0.052%) with the exception of facade M17 (step five, Δ/L=0.025%). With all facades reaching the cracked state at similar calculation steps, this suggests that there is no relationship between the overall geometry of the facade and the curvature at which it cracks sufficiently for it to effectively lose its overall stiffness.

Results summary

The results of the finite element analyses of masonry facades described here confirm the assertions discussed in the literature review (section 5.2) that facades subjected to hogging deformations act in a flexible manner once the deformations reach a certain level, due to cracking reducing their stiffness. Facades subjected to sagging deformations also crack as deformations develop, but exhibit arching which allows the facade span over sagging displacements. The finite element analyses thus confirmed that the response of facades in hogging and sagging is different. Cracking in the hogging facades is mainly vertical indicating the predominant influence of bending effects. The amount of base relative displacement at which the facades reach the cracked state is not influenced significantly by differing amounts of facade openings or the overall dimensions of the facade but is generally consistently in the range of in the range of Δ/L=0.03-0.05%. These conclusions are used below to develop a new constitutive model for surface beams which represents the behaviour of masonry facades.

5.4 Development of equivalent masonry beam model

5.4.1 Introduction

This section describes the development of a new constitutive model for surface beams which includes characteristics such that it can better model the particular actions of masonry facades when responding to ground movements. The model is called the *equivalent masonry beam* (EMB) model and is based on the equivalent elastic beam model described in section 4.3. Two approaches are considered: the main approach where equivalent masonry beams in hogging lose their bending stiffness; and an alternative approach where alternative equivalent masonry beams are given a reduced initial stiffness which increases if they go into sagging.

5.4.2 Conclusions from masonry facade analyses

The finite element analyses in section 5.3.6 above demonstrated the particular responses of masonry facades subjected to ground movements in a variety of situations. The main conclusions relevant to the development of a constitutive model for beams to represent these masonry features are that:

- Cracks develop in masonry facades as the magnitude of the strains caused by the development of curvature of the facade increases;
- Once cracked, masonry facades lose their stiffness; and
- Facades in sagging, as they crack, develop stress arches within the facade allowing them to span sagging displacements, but facades in hogging exhibit predominantly vertical cracks and do not form arches leaving any heave relatively unopposed by actions within the facade.

5.4.3 Development of EMB model

The constitutive model described here for equivalent masonry beams is based on the conclusions above. This main approach involves reducing the bending stiffness of beams going into hogging. The model has the following key components.

The equivalent masonry beam model is shown in figure 5.17. The beam has initial elastic properties based on the equivalent elastic beam method, derived from the geometry of the facade and the amount of openings as described in section 4.3. These are the flexural rigidity EI^*, the shear stiffness GA^* and the axial stiffness EA^*.

If ground displacements develop hogging curvature in the beam, once a *critical curvature*, κ_{crit}, is reached, the flexural rigidity is reduced to a small residual value to represent the loss of stiffness caused by cracking of the facade. It is not reduced completely to zero as this would cause numerical complications. The flexural rigidity is thus reduced to $f_b EI^*$ where f_b is a residual stiffness factor.

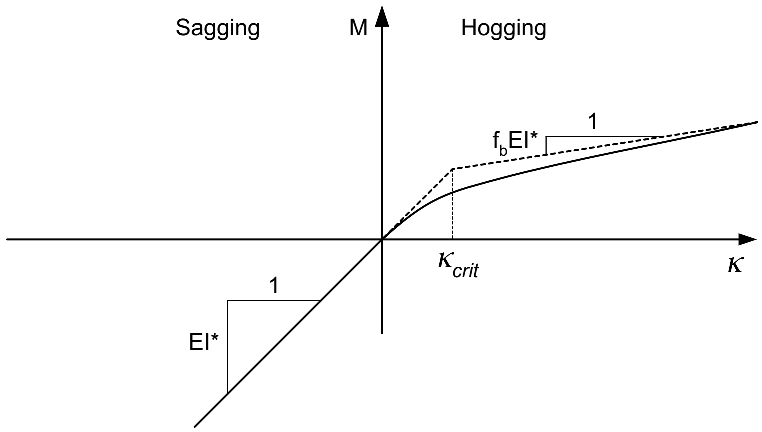

Figure 5.17: **Equivalent masonry beams in bending**

Flexural rigidity in the equivalent masonry beam model is not reduced for facades in sagging but remains set at EI^*. There is thus a non-linear elastic relationship in bending as shown in figure 5.17. This closely resembles the masonry facade constitutive model described by Liu (1997).

Another similarity to the Liu (1997) masonry facade model included here in the equivalent masonry beam model is the gradual reduction of stiffness for the beam in hogging. Gradual reduction of stiffness is included to provide a smooth transition from the 'uncracked' to the 'cracked' state (from flexural rigidity EI^* to $f_b EI^*$) for the masonry beams. This represents the physical situation where, as individual cracks develop due to increasing hogging curvature, the overall stiffness of the facade reduces. The inclusion of a smooth curve rather than a bi-linear approach also aids numerical stability during calculation.

The equations governing the gradual reduction of stiffness are similar to those used by Liu (1997) and comprise the moment-curvature relationship and its derivative

$$M = EI\kappa\left(\frac{\kappa_{crit} + f_b\kappa}{\kappa_{crit} + \kappa}\right) \tag{5.6}$$

$$\frac{dM}{d\kappa} = EI\left[\frac{1 - f_b}{\left(1 + \frac{\kappa}{\kappa_{crit}}\right)^2} + f_b\right] \tag{5.7}$$

In tunnelling simulations with staged tunnel construction, curvature of surface beams representing a building may reverse during the calculation. This might occur when transient curvatures caused by the passage of tunnel construction underneath a building are hogging but the final curvature is sagging (or vica versa). In this case, the stress path retraces the non-linear curve shown in figure 5.17.

Shear stiffness is not reduced in hogging or sagging, but takes the value as determined by the equivalent elastic beam method. This is based on the assumption that the beam's bending stiffness is lost once cracked as there is no possibility of tensile stress transfer across cracks, but that shear stiffness is retained despite the cracking due to interlock between ragged vertically cracked surfaces. Axial stiffness is also assumed to be unaffected by hogging or sagging displacements. This approach could be considered simplistic, but the equivalent masonry beam model has been developed in this way firstly to capture the principal mechanisms (cracking due to bending in hogging causing loss of bending stiffness, and arching in sagging) and secondly, to avoid over complication by including other relatively minor details (such as potential changes to shear or axial stiffness due to cracking).

5.4.4 Development of Alternative EMB model

This section describes an alternative constitutive model developed for the equivalent masonry beams. The alternative approach takes the opposite starting point to that in section 5.4.3: initially the flexural rigidity of the beam is a low value (as if the facade has already cracked). This value, EI^*_B, represents the stiffness value determined by the equivalent elastic beam approach reduced by the residual stiffness factor, f_b, as follows

$$EI^*_B = f_b EI^* \tag{5.8}$$

If the facade goes in to hogging, this reduced rigidity is maintained. In sagging however, the bending stiffness increases gradually. Under this approach the value that the beam

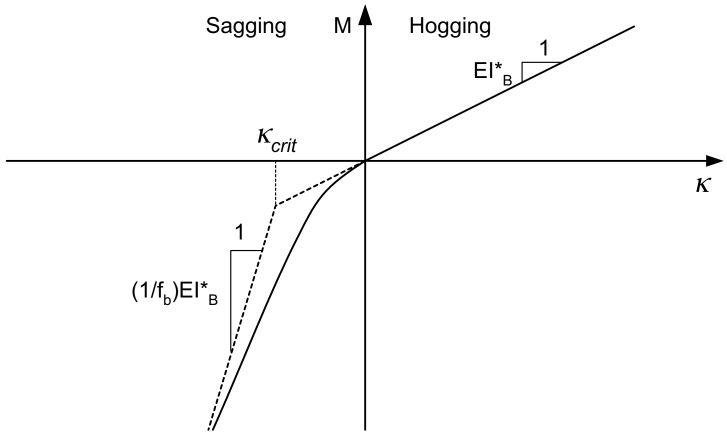

Figure 5.18: **Alternative equivalent masonry beams in bending**

stiffness approaches in sagging, is

$$\left(\frac{1}{f_b}\right) EI_B^* = EI^* \tag{5.9}$$

which is the value of bending stiffness, under by the equivalent elastic beam approach.

The alternative approach is less representative of the physical situation evident for masonry facades than the main approach which is more closely based on the conclusions from the literature and facade analysis given in section 5.4.2. That is: stiffness reduces as hogging curvature increases, replicating the loss of stiffness in the finite element analyses discussed above as Δ/L increases. The alternative approach, however, is less physically meaningful as, once the formation of arches in masonry facades in sagging had occurred, they would not gain additional stiffness as Δ/L increases. The use of the alternative approach is, however, thought to have possible advantages for numerical analysis as it may be computationally more efficient and is thus worth investigating.

The relative merits of both approaches are discussed in detail in Chapter 8 along with a discussion of appropriate values for the critical curvature (κ_{crit}) and residual bending stiffness (f_b) parameters.

5.4.5 Comparison with finite element results

There is no simple stiffness relationship (as for the elastic beams) to enable a comparison between an analytical assessment of the equivalent masonry beam model and the finite element results in the manner presented in section 4.3.3 for the elastic facades. An assessment of the equivalent masonry beams is performed following their numerical implementation in the OXFEM finite element program and is described in Chapters 7 and 8.

5.5 Conclusion

A new approach for using a non-linear elastic constitutive model to allow surface beams to model masonry facades of varying dimensions and amounts of openings more accurately has been introduced. This equivalent masonry beam model has a flexural rigidity which reduces to a low residual value in hogging to simulate the relatively flexible response of a cracked facade in that state. Bending stiffness is retained in sagging to simulate a rigid arching response. Axial and shear properties are linearly elastic. This model is shown to be equally valid for both a smooth or a rough base boundary condition assumption.

This approach is based on the conclusions of the discussion of masonry facades in the literature review in this Chapter as well as the results of the finite element analyses of masonry walls and facades undertaken for this study.

It is important to note that the developments described in Chapters 4 and 5 have been developed based on analyses of the response of elastic and masonry walls and facades subjected to *imposed* ground displacements. The results of these analyses thus do not include soil-structure interaction effects, being isolated analyses with the building alone subject to imposed displacements.

Following the implementation of new beam elements and the equivalent beam models into the finite element program OXFEM, described in Chapter 6, analyses including soil-structure interaction are undertaken in Chapter 8 where the new beams are used to represent masonry facades in three-dimensional analyses of building response to tunnelling.